Spin pumping investigations in halfmetallic doped Manganese Oxide

Author:
Lennart de Bruin
0984329

Supervisors:
Tim Verhagen, MSc.
Prof. Dr. Jan Aarts

Faculty of Science,
Leiden University

August 14, 2012

Samples grown by:
Ishrat Mubeen, MSc.
Daan Boltje

Contents

Chapter 1

Introduction

When looking at a charge current at subnanometer scale, the current is propagated by electrons, colliding with lattice imperfections. These collisions lead to a change in momentum, which causes resistance. This generates Joule heat, seen as a loss of kinetic energy of the electrons in the current itself. The heat is a problem for the technological advancement in producing increasingly smaller electronics.

1.1 Spin currents

One way to counter the generation of heat in charge currents is using the spin angular momentum of electrons instead of the translational momentum and transport only the spin but not the charge of the electron. If the spin of the electrons in the current is polarised, a spin current can be made.

A charge current can be defined as $\mathbf{J}_q = \mathbf{J}_\uparrow + \mathbf{J}_\downarrow$, where $\mathbf{J}_{\uparrow/\downarrow}$ is the total charge current of the spins in the $\uparrow / \downarrow$-direction. A spin current is defined as $\mathbf{J}_s = -\frac{\hbar}{2e}\left(\mathbf{J}_\uparrow - \mathbf{J}_\downarrow\right)$. If $\mathbf{J}_\uparrow = -\mathbf{J}_\downarrow$, the spin polarised current is a pure spin current. A pure spin current is time reversal independent, which causes it to be transported without resistance[1]. This property of pure spin currents can be used for applications such as low-heat, power efficient spin-based electronics, called spintronics.

The field of spintronics consists of two parts; generating a spin polarised current and retaining the spin polarisation of that current. To retain the orientation of the spins of the electrons, light materials are used, of which the atoms do not easily couple to the spins, causing the spin to be randomised only slowly.

To generate a spin current, ferromagnets are used. Different principles —such as the spin Seebeck effect, or the spin Hall effect— can then be utilised to extract a pure spin current from the ferromagnet. Another way to induce a pure spin current is by a process called spin pumping. This requires that there is a normal metal adjacent to the ferromagnet. The spin current will then flow from the ferromagnet into the normal metal.

Just as the ability to retain the spin polarisation depends on the material that the electron flows through, the ability to generate a spin polarised current depends on the material of the ferromagnet. Moreover, the interface between the two layers determines whether the spins from the ferromagnet reach the normal metal.

1.2 Manganese oxides

Almost any ferromagnet can be used to generate a pure spin current. However, an interesting group of materials for the purpose of spin pumping is the group of transition metal oxides. These oxides can have a range of different physical properties, depending on the base transition metal used, and the element used for doping the oxide with. Some of these properties are ferromagnetism, ferroelectricity, antiferromagnetism, superconductivity, metallicity and half-metallicity.

Here we concentrate on oxides with a perovskite structure, with a chemical formula of ABO_3. It is a body-centered cubic structure with the oxygen atoms forming an octahedron around the base atom. The A-sites of ABO_3 are at the corners of the body-centered cubic structure, and the B-site is at the position of the base atom. The pseudocubic structure of bulk is shown in Fig. 1.1.
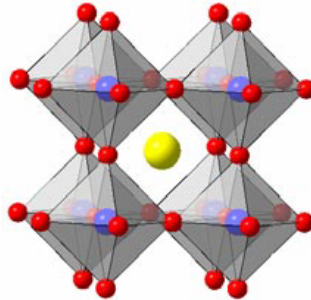

Figure 1.1: The perovskite structure of bulk ABO_3 (pseudocubic). In the case of Lanthanum Manganese Oxide, $LaMnO_3$, the base atom at the B-site is Manganese atoms, which is coloured yellow, the Oxygen atoms are red and the Lanthanum atoms at the B-sites are blue. From [2].

Lanthanum Manganese Oxide, $LaMnO_3$, has such a perovskite structure, with Manganese as base atom. It is an antiferromagnetic insulator with a Néel temperature of 150K.

$LaMnO_3$ can be doped with another element. This means that the Lanthanum atoms are replaced by this doping element. Doping $LaMnO_3$ with Strontium will give it a range of different physical properties, depending on the amount of doping. This can be seen in Fig. 1.2.

The reason for this is that doping with Sr changes the number of valence electrons available and so the occupancy of the energy levels in the material.

Interestingly, doping $LaMnO_3$ with 30% Sr, $La_{0.7}Sr_{0.3}MnO_3$ (henceforth called LSMO), makes it a ferromagnetic conductor, and gives it a high Curie temperature of 369 K[4]. But the most prominent property is the fact that it becomes a half-metal[5]; the spin polarisation is 100%. This in contrast with simple transition-metal ferromagnets, such as Fe, which have a spin polarisation of only 40%[6].

This 100% spin polarisation is attributed to the double exchange mechanism, which only allows electrons with spin up to be conducted from Manganese atom to Manganese atom through an Oxygen atom. This mechanism is also the cause of so called colossal Magnetoresistance behaviour.
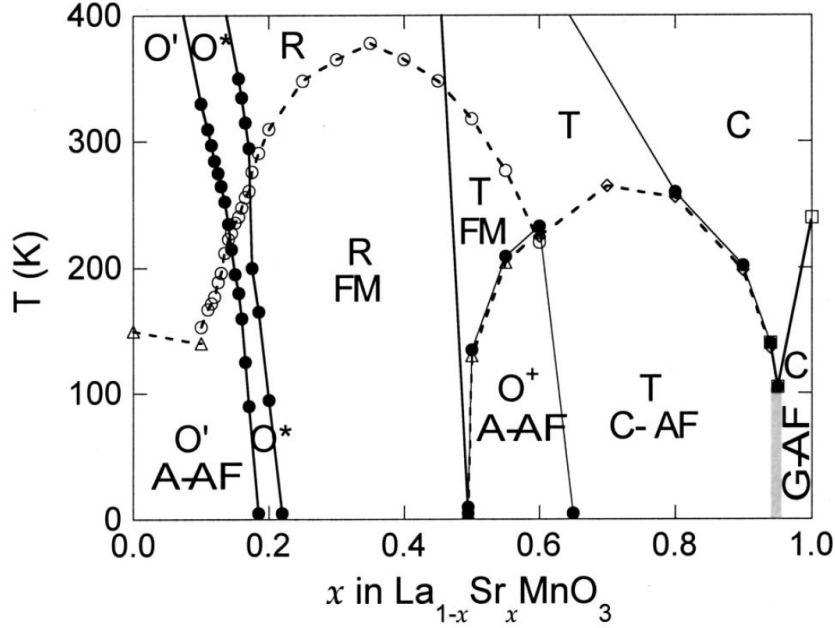
Figure 1.2: The doping phase diagram of $La_{1-x}Sr_xMnO_3$. The symbols denote the magnetic ordering. The letters A, R, C, O and T have to do with the crystalline and magnetic order, FM means ferromagnetic metal and AF means antiferromagnetic. The temperature on the y-axis is the Néel or Curie temperature of the particular composition. From [3].

1.3 Thin LSMO films

Thin films of a certain material have to be grown on a substrate. This also means that, if these do not have the same lattice parameters, the lattice parameters of the material will be stretched or compressed in order to fit the substrate's. This causes strain in the film.

The amount of strain depends on: the lattice mismatch of the film with respect to the substrate; the thickness of the film; the direction of the film with respect to the substrate; and the structure of both the film and the substrate.

Strain can affect numerous properties of the material, e.g. magnetisation, transport properties, the Curie temperature T_C and the way (magnetic) domains are formed. This is also the case for LSMO, which seems particularly sensitive to strain.

LSMO thin films have a lower T_C than bulk LSMO, depending on the type of substrate. Using $NdGaO_3$ (NGO) as a substrate causes the T_C to drop to a value which is still above room temperature, which is advantageous for measuring and perhaps for use in spintronics devices. Similar perovskite substrates, like $SrTiO_3$, cause the LSMO to have much lower T_Cs. The reason for the higher T_C for LSMO on NGO is the small lattice mismatch of bulk LSMO (a = 3.87 Å) and (001)-oriented NGO (a = 5.43 Å, b = 5.50 Å, c = 7.71 Å).

The lattice mismatch is calculated by $m = \frac{a_{NGO} - a_{LSMO}}{a_{LSMO}}\%$. For epitaxial LSMO on (001) NGO, this is -1.11% in the [110] direction, and 0.16% in the [1$\bar{1}$0] direction [7].

1.4   This project

It is thus far not known whether a spin current can be induced from LSMO thin films. The interface between LSMO and the adjacent layer of normal metal is a major issue. The Fermi energies line up in a metallic contact, allowing for spins to be transported into the normal metal. However, it is not known whether the quality of the LSMO is good enough to still be metallic at the interface.

In this project an effort is done to check whether it is possible to induce a spin polarised current from LSMO on NGO. This is done by comparing the linewidths of single films of LSMO with LSMO|Cu and LSMO|Pt bilayers. The linewidth of LSMO|Cu should not be much broader than that of the single layer LSMO. However, a significant broadening in the LSMO|Pt results would indicate that spins have been pumped into the Pt layer.

Chapter 2 explains the theory of EPR/FMR and spin pumping. Chapter 3 gives information about the sample growth and characterisation, measurement equipment and how the measurements are conducted. Chapter 4 contains the obtained results. Chapter 5 contains the discussion of these measurements and results. Chapter 6 contains several conclusions drawn from both the measurements and the discussion.

Chapter 2

Theory

This chapter describes the theory needed for the experiment. It covers Electron Paramagnetic Resonance (EPR), Ferromagnetic Resonance (FMR) and intrinsic and extrinsic damping of FMR, which includes spin pumping. The free energy in the ferromagnet and the magnetic anisotropy will also be discussed, which are important for LSMO, and finally the Inverse Spin Hall Effect (ISHE) will be described.

2.1   Electron Paramagnetic Resonance

Electron Paramagnetic Resonance is a spectroscopy technique that relies on unpaired electrons.

The origin of EPR spectroscopy lies in the degeneracy of the energy of the states with the m_s quantum number. If an external magnetic field H_0 is applied, the states will split into $2s + 1$ states. In the case of electrons, $s = 1/2$, and thus there are two states, $m_s = +1/2$ and $m_s = -1/2$; or up and down. This can be seen in Fig. 2.1.
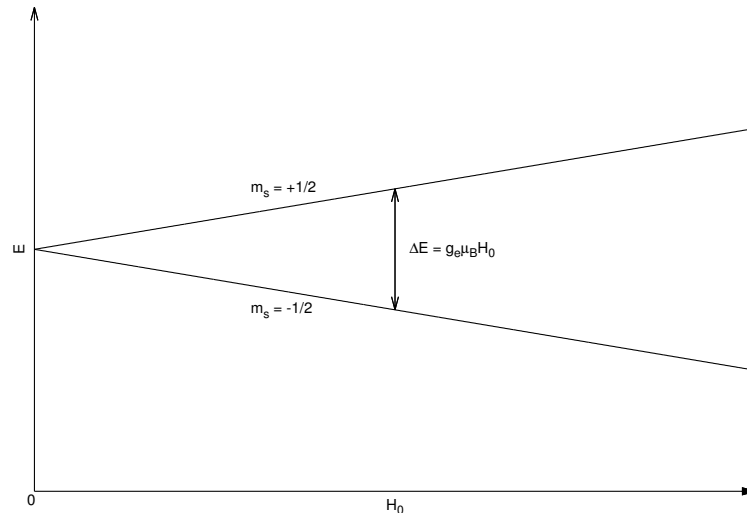
Figure 2.1: Lifting the degeneracy in the m_s quantum number by applying an external magnetic field yields Zeeman splitting, illustrated here by plotting the energies of the two m_s-states as a function of the applied magnetic field H_0.

The external magnetic field H_0 splits the energy into two distinct states, with energy $E_\pm = \pm\frac{1}{2}g_{\text{eff}}\mu_B H_0$. Here, g_{eff} is the effective Landé g-factor of the electrons in the material

and μ_B is the Bohr magneton. The difference of energy between the two states is $\Delta E = E_+ - E_- = g_{\text{eff}}\mu_B H_0$.

If the energy of the photons of the externally applied microwave radiation is equal to this energy difference, the electrons in the material will be excited from the down-state to the up-state. The strength of field H_0 at which this happens is called the resonance field, H_r. The fundamental equation of EPR applies here:

$$h\nu = \Delta E = g_{\text{eff}}\mu_B H_r, \tag{2.1.1}$$

where h is Planck's constant, and ν is the frequency of the microwave radiation. In an EPR experiment, the frequency ν is usually held fixed while the field is swept through the resonance condition.

2.2 Ferromagnetic Resonance

Ferromagnetic resonance is similar to EPR. The spins in a ferromagnet are coupled via the exchange energy, and the whole system can be considered as a macrospin. The entire magnetisation $\mathbf{M}$ of the ferromagnet will then precess around the effective magnetic field $\mathbf{H}_{\text{eff}}$. This field is determined by:

$$\mathbf{H}_{\text{eff}} = \mathbf{H}_0 + \mathbf{h}_{\text{rf}} + \mathbf{h}_{\text{d}} + \mathbf{H}_{\text{K}} + \mathbf{h}_{\text{ex}} + \mathbf{h}_{\text{G}} \tag{2.2.1}$$

Here, $\mathbf{H}_0$ is the external field, $\mathbf{h}_{\text{rf}}$ is the magnetic field of the microwave radiation, $\mathbf{h}_{\text{d}}$ is the demagnetising field, $\mathbf{H}_{\text{K}}$ is the magnetocrystalline anisotropy field, $\mathbf{h}_{\text{ex}}$ is the exchange field, induced by the relative orientation of spins in the material, and $\mathbf{h}_{\text{G}}$ is the magnetic damping field[8].

The precessing magnetisation is described by the Landau-Lifschitz-Gilbert equation:

$$\frac{d\mathbf{M}}{dt} = -\gamma\mathbf{M} \times \mathbf{H}_{\text{eff}} + \alpha\mathbf{M} \times \frac{d\mathbf{M}}{dt} \tag{2.2.2}$$

The first term describes the precessing magnetisation, where γ is the gyromagnetic ratio, given by $\gamma = g_{\text{eff}}\mu_B/\hbar$. The second term describes damping , where α is called the damping parameter, and contains all the different types of damping of the magnetisation.

The magnetisation vector can be seen as precessing around the effective field $\mathbf{H}_{\text{eff}}$. The damping will then cause the magnetisation to fall inward onto the field vector. This can be seen schematically in Fig. 2.2.

Equation (2.2.2) can be solved analytically, as done in [8], but the free energy density F in the ferromagnet can also be used to extract information, as explained in section 2.6.

2.3 Damping

Because a precessing magnetisation is in a higher energy state than a static magnetisation, and nature seeks the lowest energy state possible, the ferromagnet will try to decrease its internal energy. This is called damping, and the ferromagnet can do this in various ways. Damping of the precessing magnetisation increases the total, peak-to-peak, linewidth ΔH_{pp} of the FMR signal.
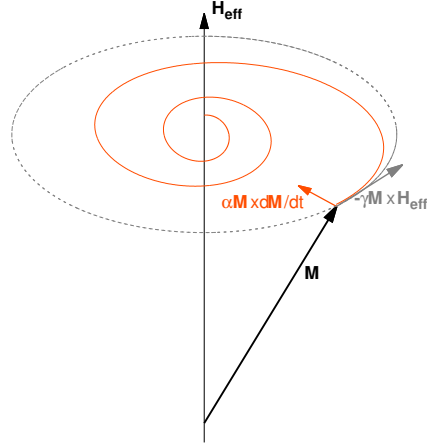
Figure 2.2: Illustration of the Landau-Lifschtiz-Gilbert equation. The magnetisation precesses around the external effective magnetic field. It is damped by the damping term, which points inwards, causing the magnetisation to spiral towards the center.

The damping parameter α in Eq. (2.2.2) contains all possible damping contributions. A few of these are:

Intrinsic damping This is caused by spin-orbit coupling in the ferromagnet itself, and therefore depends on the material of the ferromagnet. Intrinsic damping is also dependent on the frequency of the magnetic field of the microwave radiation, $\mathbf{h}_{rf}$; and causes the linewidth to increase according to $\Delta H_{pp} \sim \frac{\alpha}{\gamma} f$ [9].

Damping by eddy currents If a film is thick enough ($d \gtrsim 50$ nm), eddy currents, which are current vortices, can appear in the ferromagnet.

Damping by exerting a pure spin current This is called spin pumping. This constitudes most of this research, and is described in the following section. Damping of this kind causes the linewidth to increase linearly with α [10].

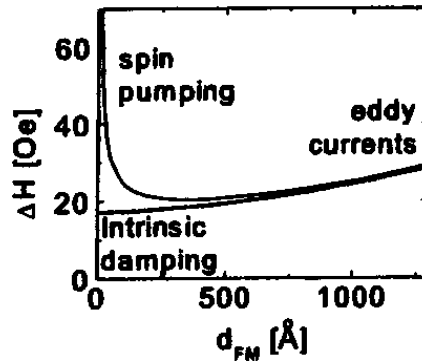These contributions are shown in Fig. 2.3.

Figure 2.3: Typical linewidth dependence ΔH_{pp} as a function of the thickness of the ferromagnetic film d_{FM}. The different contributions are indicated. From [11].

2.4   Spin pumping

Another way for the ferromagnet to decrease its internal energy is by ejecting spins, in the case that the ferromagnet has an adjacent layer of normal metal. The spins will then flow into the normal metal. There, their spins can be flipped around, after which they can flow back into the ferromagnet. If the phase of the spins is different from the phase of the spins in the ferromagnet, this can be seen as damping of the magnetisation. The flow of spins leaving the ferromagnet is polarised in the direction of **M**. This entire process lowers the magnetisation of the ferromagnet, and thus lowers the total internal energy. This is shown schematically in Fig. 2.4.
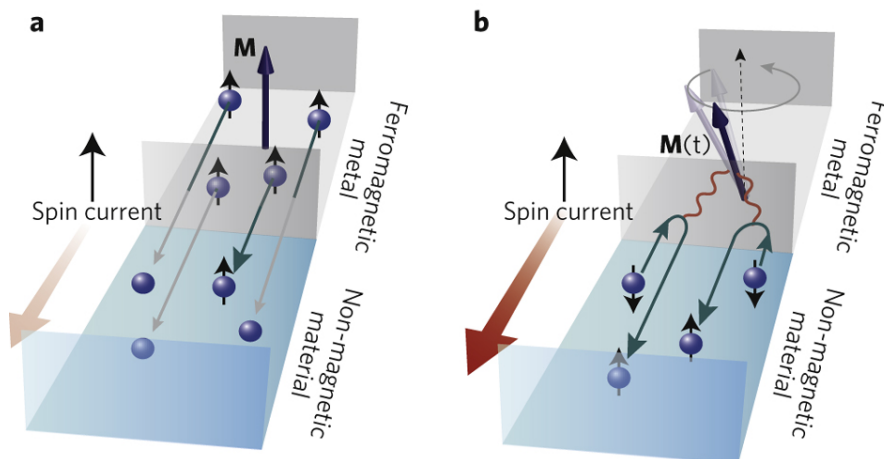

Figure 2.4: Schematic depiction of the process of spin pumping. **a**) shows a static magnetisation, which by itself causes a small net spin current. **b**) shows a precessing magnetisation, which exerts a bigger spin current and flips spins flowing back, lowering the magnetisation. From [12].

The amount of spin-flips in the normal metal depends on spin-orbit coupling, with Hamiltonian H_{SO}. Since $H_{SO} \sim Z^4$, where Z is the atomic number, the ease of spin-flips depends heavily on the mass of the atoms in the metal. When the atoms of the metal are heavy, for example Pt, so that spins easily flip, the metal is called a good spin sink. Conversely, if the atoms are light, the spins don't flip, and the material is called a bad spin sink, for example Cu.

If spins flip easily, as a consequence, they do not accumulate at the interface of ferromagnet|normal metal, however, they cannot penetrate the metal deeply either. In other words, the spin coherence length is short. Otherwise, if spins do not flip easily, they can accumulate at the interface. If there is an accumulation of spins at the interface, spins can be reflected back into the ferromagnet, effectively diminishing the damping.

The pumped spin current itself is described by[10]

$$\mathbf{I}_s^{\text{pump}} \sim g_r^{\uparrow\downarrow} \mathbf{M} \times \frac{d\mathbf{M}}{dt} - g_i^{\uparrow\downarrow} \frac{d\mathbf{M}}{dt}. \tag{2.4.1}$$

Here, $g_r^{\uparrow\downarrow}$ and $g_i^{\uparrow\downarrow}$ are the real and imaginary spin mixing parameters at the interface, respectively. They depend on the reflection and transmission coefficients of up and down spins at the interface.

2.5 Magnetic anisotropy

Magnetic anisotropy occurs when it is energetically favorable for electron spins to be in a certain direction. This also depends on the structure and the symmetry of the material, in other words, crystalline anisotropy; the shape of the material/sample, in other words, shape anisotropy; and strain-induced anisotropy[7].

The anisotropic energy is the energy which is needed to move the magnetisation of the material away from one of the anisotropic axes. It contributes to the total free energy in the ferromagnet, given by an in-plane and out-of-plane component:

$$E_{\text{anisotropy}} \sim K^{//} + K^{\perp}, \tag{2.5.1}$$

where $K^{//}$ is the parallel anisotropy constant, and $K^{\perp}$ is the perpendicular anisotropy constant.

2.6 Free energy

The free energy density F is given by[13]:

$$
\begin{aligned}
F = E/V &= F_{\text{Zeeman}} + F_{\text{demagn.}} + F_{\text{out-of-p.an.}} + F_{\text{in-p.an.}} \\
&= -M_s \left\{ \cos\theta_M \cos\theta_H \cos\varphi_M + \sin\theta_M \sin\theta_H \right\} \\
&\quad - \left(2\pi M_s^2 - K^{\perp} \right) \cos^2\theta_M \\
&\quad - \tfrac{1}{8} K^{//} \left\{ 3 + \cos\left(\varphi_M - \varphi_{K^{//}}\right) \right\} \cos^4\theta_M.
\end{aligned}
\tag{2.6.1}
$$

Here, V is the volume of the ferromagnetic layer, $F_{\text{demagn.}}$ is the demagnetisation free energy density, $F_{\text{in-p.an.}}$ and $F_{\text{out-of-p.an.}}$ are the in- and out-of-plane anisotropy free energy densities, respectively, M_s is the saturation magnetisation. The angles are shown in Fig. 2.5.
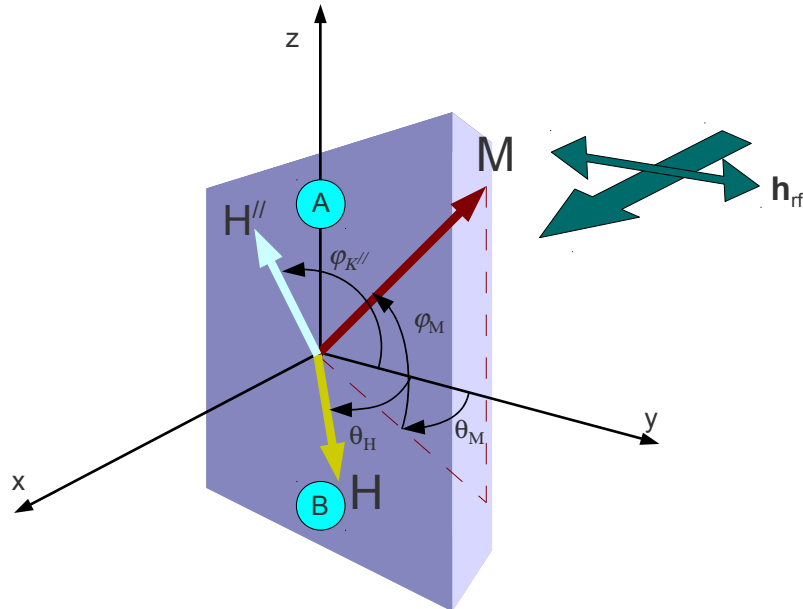

Figure 2.5: The coordinate system used for the free energy. Electrodes, to measure the inverse spin Hall voltage, are put on sites A and B.

The resonance frequency ω_r of the precessing magnetisation is given by

$$\left(\frac{\omega_r}{\gamma}\right)^2 = \left(\frac{1}{2\pi}\right)^2 \frac{1}{M_s^2 \cos^2 \theta_M} \left[\frac{\partial^2 F}{\partial \theta_M^2}\frac{\partial^2 F}{\partial \varphi_M^2} - \left(\frac{\partial^2 F}{\partial \theta_M \partial \varphi_M}\right)^2\right]. \tag{2.6.2}$$

The linewidth can be written as

$$\Delta H_{pp} = \Delta H_{pp}^{\text{hom.}} + \Delta H_{pp}^{\text{inhom.}}, \tag{2.6.3}$$

where $\Delta H_{pp}^{\text{hom.}}$ is the homogeneous increase in linewidth, containing the increase due to spin pumping, and $\Delta H_{pp}^{\text{inhom.}}$ is the increase in linewidth due to inhomogeneities in the material.

At resonance $H = H_r$ and θ_M and φ_M are determined by $\frac{\partial F}{\partial \theta_M} = 0$ and $\frac{\partial F}{\partial \varphi_M} = 0$. The homogeneous part of the increase in linewidth can then be expressed as[14]:

$$\Delta H_{pp}^{\text{hom.}} = \frac{\alpha}{M_s}\left(\frac{\partial^2 F}{\partial \theta_M^2} + \frac{1}{\cos^2 \theta_M}\frac{\partial^2 F}{\partial \varphi_M^2}\right)\left|\frac{d(\omega_r/\gamma)}{dH_r}\right|^{-1}. \tag{2.6.4}$$

The linewidth due to inhomogeneities can be expressed as

$$\Delta H_{pp}^{\text{inhom.}} = \left|\frac{dH_r}{d(4\pi M_{\text{eff}})}\right|\Delta(4\pi M_{\text{eff}}) + \left|\frac{dH_r}{d\theta_H}\right|\Delta\theta_H, \tag{2.6.5}$$

where $\Delta(4\pi M_{\text{eff}})$ and $\Delta\theta_H$ are the distribution of M_{eff} and θ_H in the film, respectively.

Measuring the linewidth as a function of θ_H will give the linewidth due to inhomogeneities, an important aspect of LSMO, which is very sensitive to disturbances in its internal structure.

2.7   Inverse Spin Hall Effect

The Inverse Spin Hall Effect describes how a charge current $\mathbf{J}_q$ is produced by a spin current $\mathbf{J}_s$. The underlying mechanism is spin-orbit coupling and the asymmetric deflection of up and down spins[15, 16].

The induced charge current gives rise to an electric field, given by[17]:

$$\mathbf{E}_{\text{ISH}} \sim \mathbf{J}_s \times \boldsymbol{\sigma}. \tag{2.7.1}$$

Here, $\boldsymbol{\sigma}$ is the direction of the spin polarisation. This electric field in turn induces a measurable voltage, according to $V_{\text{ISH}} = w_{el}|\mathbf{E}_{\text{ISH}}|$, where w_{el} is the width between the two electrodes to measure the voltage. The effect is depicted schematically in Fig. 2.6. The measurement of the inverse spin Hall voltage is described in section 3.2.3.
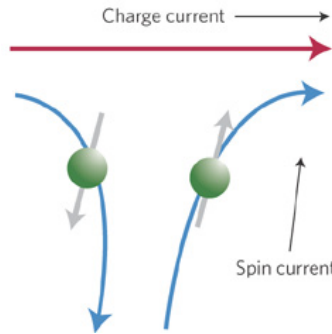

Figure 2.6: Schematic depiction of the process of the inverse spin Hall effect. From [18].

Chapter 3

Experimental

This chapter describes the experimental side of this reseach. This constitutes: the sample growth and preparation, the used measurement set-ups and the application of the theory described in the previous chapter.

3.1 Growth of LSMO

A layer of 10 nm to 13 nm thick LSMO was deposited epitaxially, by sputtering in an Oxygen atmosphere, on 8 mm × 8 mm or 10 mm × 10 mm and 0.5 mm thick NGO (001) orthorhombic substrates supplied by CrysTec, at a temperature of 840 °C, and a pressure of 2.2-2.3 mbar.

It is not known how these substrates are terminated; the final layer —the layer adjacent to the LSMO layer— could be either $NdO_{1+\delta}$ (single terminated) or $GaO_{2-\delta}$ (double terminated).

The samples were then cooled down in vacuum to a lower temperature, depending on the sample. Then Cu or Pt was deposited on it, in an Argon atmosphere. The samples were then cut into pieces of ∼2 mm × 2 mm. For each sample, the growth parameters can be found in appendix B.

3.2 Measurements/Methods

3.2.1 Electron Paramagnetic Resonance

Equipment

EPR measurements were done using a Bruker EMX spectrometer, equipped with an ER 070 magnet and an ER 4119HS microwave cavity.

Set-up

EPR/FMR is the most important method of measuring used in this research. A typical EPR set-up is shown in Fig. 3.1.

A sample is put inside a cavity located in a uniform dc magnetic field, $\mathbf{H}_0$. This magnetic field is modulated with a certain amplitude and frequency. Microwaves are generated and sent through a waveguide, via a circulator, to the cavity, where they form a standing wave. The sample will be located in the cavity in such a way, that it is in a node of the electric field and an antinode of the magnetic field. Part of the microwave
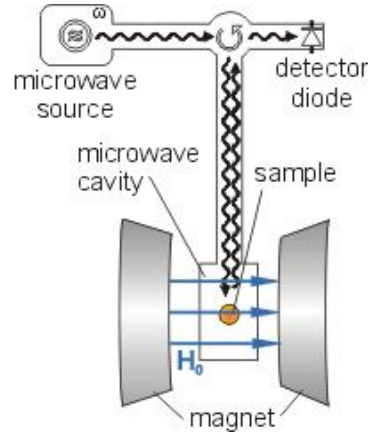
Figure 3.1: Schematic view of an EPR setup. From [19].

radiation will travel back into the waveguide and, via the circulator, end up on a diode, which registers the amount of radiation left.

At $\theta_H = 0°$, the sample is in-plane with the magnetic field $\mathbf{H}_0$. It can be rotated out-of-plane by rotating the sampleholder. At $\theta_H = 90°$, the sample is completely out-of-plane. Unfortunately, the sample can not be rotated in-plane.

Technical details

The frequency of the microwave radiation is in the X-band, at ~9.8 GHz. This frequency can not be changed. The attenuation used is 10 dBm to 20 dBm. The modulation frequency is always 100 kHz and the modulation amplitude is 20 G. The time constant used was 2.56 ms or 5.12 ms, and the conversion time is between 15 ms and 40 ms.

Fig. 3.2 shows a sampleholder with a sample on it. The sampleholders are made from one piece of Rexolite and a cut-out is made to place the sample in. The samples were glued onto the sampleholder by using silver paint.
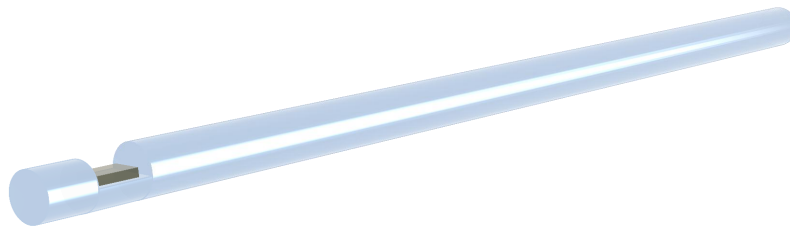

Figure 3.2: One of the sampleholders used. The sample is located in the cut-out of the cylinder, glued on with silver paint.

Operation

The strength of the external field, H_0, is swept from 0 to $H_{\max}$, while subjecting the electrons in the sample to microwave radiation. The electrons can absorb this radiation, and be excited. The absorption spectrum is a function of the external field strength, $A(H_0)$.

This spectrum has, in the case of a ferromagnet, the shape of a Lorentzian. However, since a lock-in detection is used in the setup, the output is the derivative of the absorption

to the external field, $\frac{dA}{dH}$, and is thus the derivative of a Lorentzian. This is shown in Fig. 3.3.
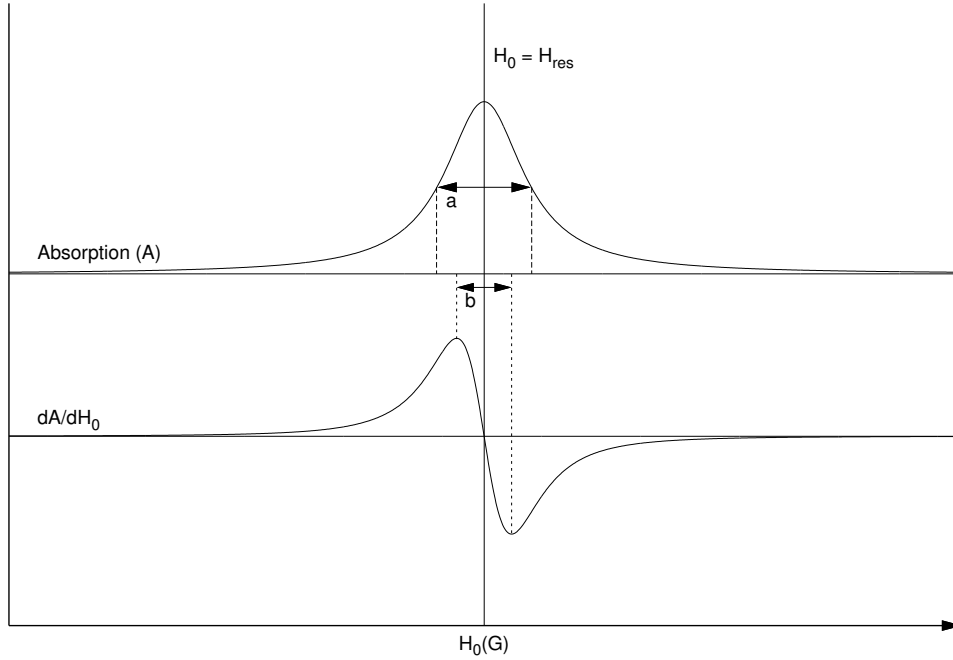

Figure 3.3: Example of the EPR signal of a ferromagnet. The arrows denote the width between the half of the maximum value of the Lorentzian (a) and the width between the extreme values of the derivate of the Lorentzian (b). The width of a is $\sqrt{3}$ times that of b.

The linewidth, ΔH_{pp}, is defined to be the width at half height of the Lorentzian, in millitesla, which is the distance between the extreme values of the derivative $\frac{dA}{dH}$ multiplied with $\sqrt{3}$.

The sample was rotated out of the plane of the external field while measuring the linewidth. This is defined as the angular dependence of the linewidth.

3.2.2 Magnetisation

Magnetisation measurements were done using a Quantum Design MPMS-5S. This SQUID measures the magnetic moment in emu. This is converted to μ_B/Mn atom by:

$$
\begin{aligned}
\text{signal [emu]} \quad &= \quad \text{signal} \cdot 10^{-3} & [\text{A} \cdot \text{m}^2] \\
&= \quad \text{signal}/(1.078 \cdot 10^{26}) & [\mu_B] \\
&= \quad \text{signal}/(1.078 \cdot 10^{26} \cdot V_{\text{LSMO}}/V_{\text{u.c.}}) & [\mu_B/\text{Mn atom}]
\end{aligned}
$$

Here, V_{LSMO} is the total volume of the LSMO layer, and $V_{\text{u.c.}}$ is the volume of an LSMO unit cell.

3.2.3 Inverse spin Hall effect

To measure the inverse spin Hall voltage induced by the spin current, two electrodes are put on the sample —one on site A and one on site B, in Fig. 2.5. These electrodes are copper wire glued on by silver paint. These wires run along the sample holder and —with a connector— are put into a nanovoltage meter.

Chapter 4

Results

In this chapter the measurements are shown and briefly discussed. For each sample the topography and the saturation magnetisation were determined. For most samples the angular dependence of the linewidth is also shown.

Samples are named like NL1, which stands for N(GO)L(SMO)identifier. At the beginning of each section, the full name, including the thickness of each layer, is shown. If the identifier has the letter m in it, that means that it is a piece cut from the middle of the larger sample. The structure of this is taken to be uniform. If the identifier has an s in it, this means that the piece is from the side of the larger sample. It is not known whether these samples are uniform.

Extra information about the samples —for example, dimensions, roughness, etc.— can be found in Appendix A.

4.1 NL1

This sample is layered as NGO|LSMO(13nm). The purpose of measuring this sample is to determine the various basic parameters of LSMO on NGO, such as the topography, the magnetisation as a function of the external field, the magnetisation as a function of temperature, and the angular dependence of the FMR linewidth.

4.1.1 Topography

The topography of NL1 measured by Atomic Force Microscopy (AFM) is shown in Fig. 4.1.1. One can see that the overall surface is smooth, however, there are a few specks of dust or dirt on it.
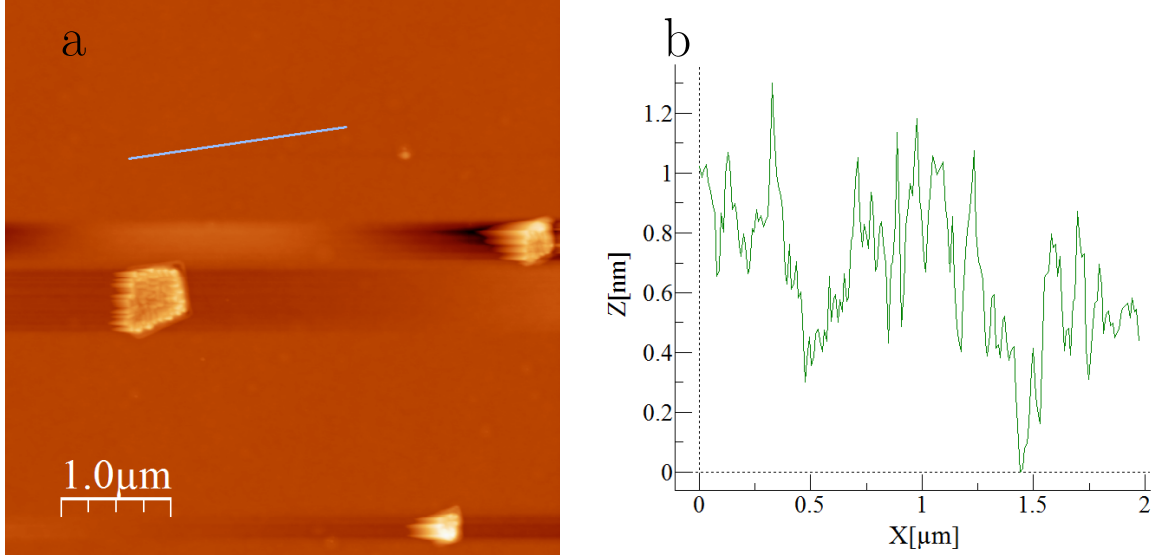
Figure 4.1.1: (a) The topography of NL1. (b) The height variations along the line drawn in (a). The roughness is 0.33 nm.

4.1.2 Magnetisation measurements

In Fig. 4.1.2 the magnetisation of NL1 is plotted as a function of the temperature. This measurement was done in an external magnetic field of 0.6 mT. The Curie temperature is shown to be $\sim$ 320 K. Afterwards, the sample was rotated in-plane by 90° and the measurement was repeated. This is also shown in Fig. 4.1.2.
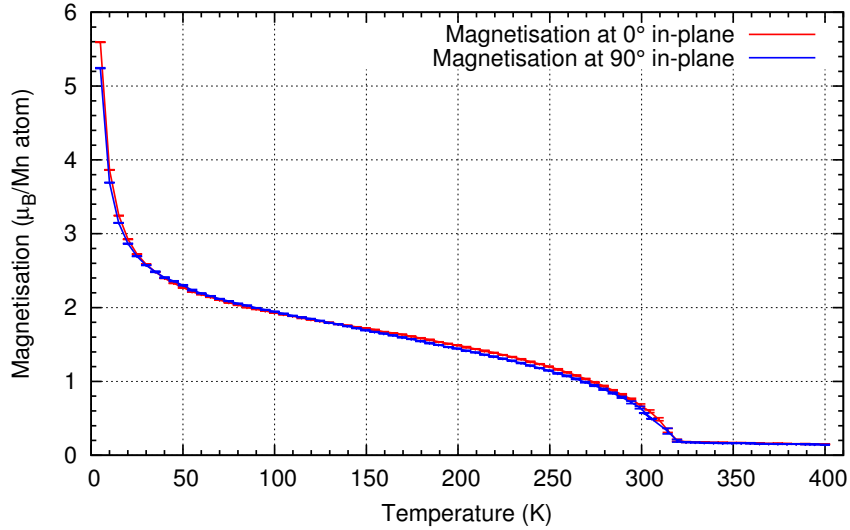

Figure 4.1.2: The magnetisation vs. temperature of NL1-4(s) in an external field of 0.6 mT. The T_C is 320 K.

To determine the coercive field and the saturation magnetisation, the magnetisation was measured as function of the external field, at a temperature of 10 K. Afterwards, the sample was rotated in-plane by 90°. The measurement was done at a temperature of 300 K. This is shown in Fig. 4.1.3 and 4.1.4, respectively.
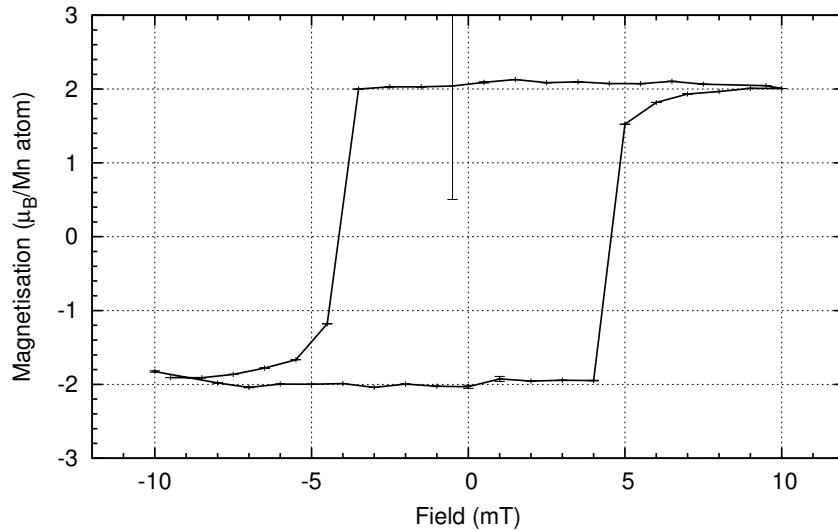
Figure 4.1.3: The magnetisation of NL1-4(s) at a temperature of 10 K. The saturation magnetisation is 2 μ_B/Mn atom.
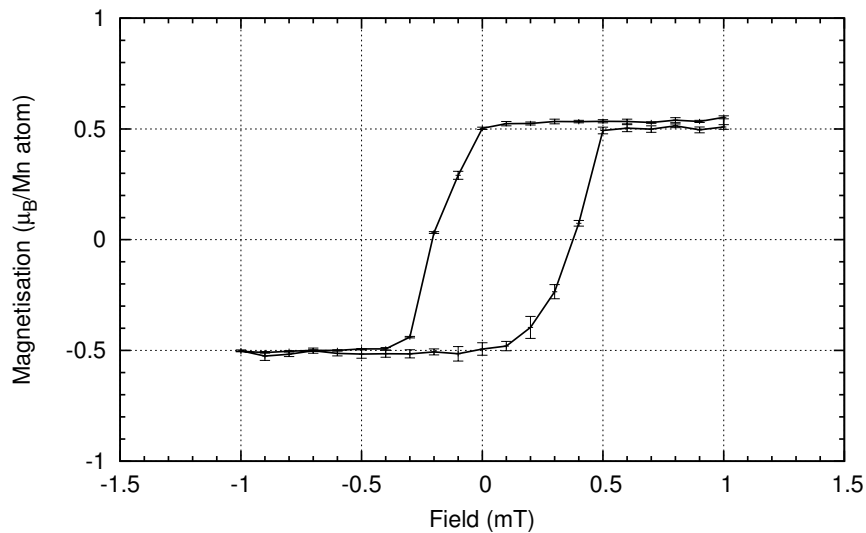

Figure 4.1.4: The magnetisation of NL1-4(s) at a temperature of 300 K. The saturation magnetisation is 0.5 μ_B/Mn atom.

4.1.3 FMR measurements

A few different FMR spectra of NL1-6(m) are shown in Fig. 4.1.5. All of these spectra were measured at room temperature.
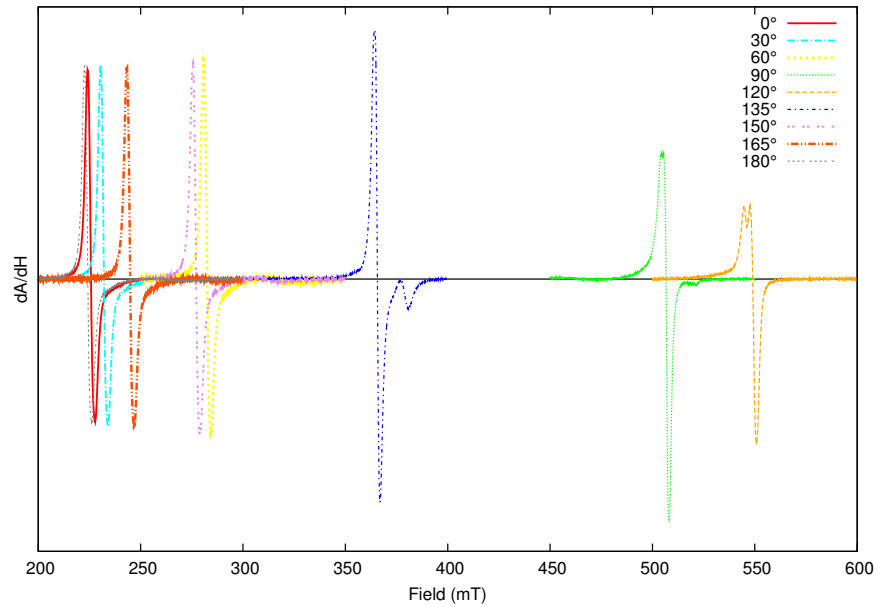
Figure 4.1.5: FMR spectra of NL1-6(m) at different out-of-plane angles at 293 K.

The angular dependence of linewidth is shown in Fig. 4.1.6. Rotating the sample by 90° in-plane gives no notable difference in the linewidth and is therefore not shown here, nor has it been measured for subsequent samples.
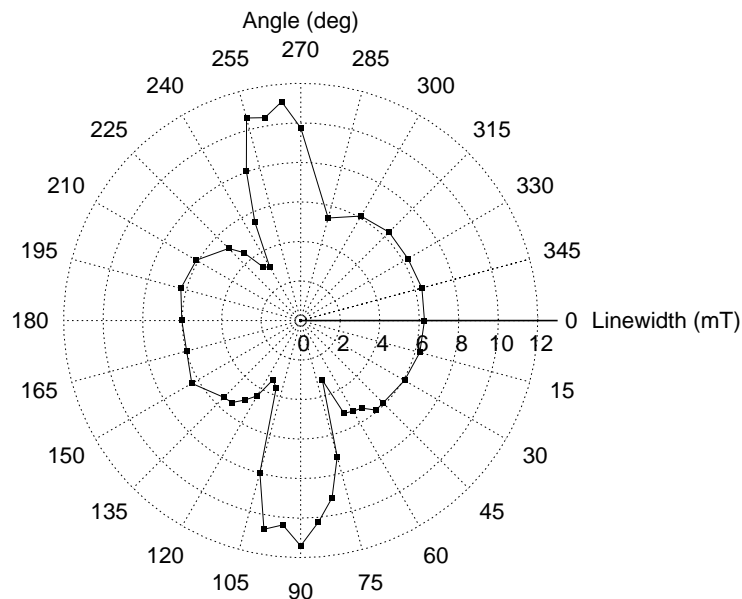

Figure 4.1.6: Angular dependence of linewidth of NL1-6(m) at a temperature of 293 K.

The angular dependence of the resonance field was also measured at room temperature and is shown in Fig. 4.1.7.
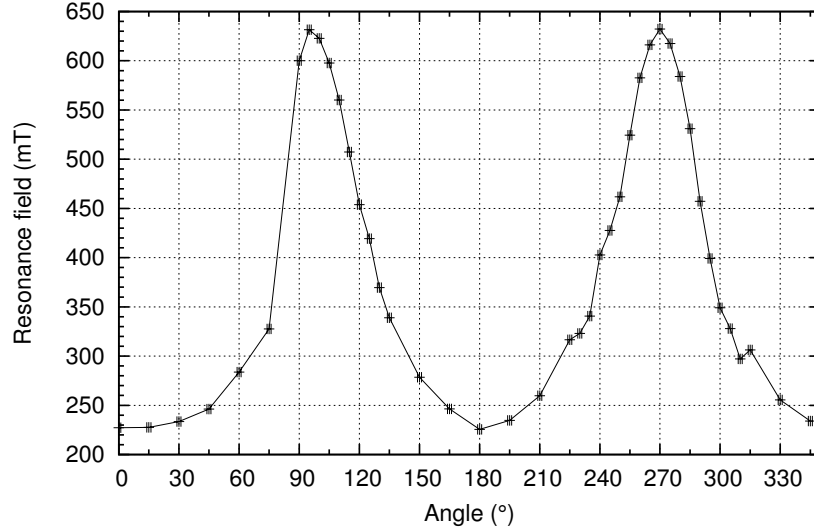
Figure 4.1.7: Angular dependence of resonance field of NL1-6(m) at a temperature of 293 K.

4.1.4 Discussion of NL1

This sample has a very small RMS roughness, of 0.33 nm. The magnetisation saturation M_s is 2 μ_B/Mn atom, which differs from the theoretical value of 3.5 μ_B/Mn atom, which indicates a dead layer. There are significant differences in the resonance field H_r, from 230 mT in-plane, to 630 mT out-of-plane. The angular dependence of linewidth also differs, from 6.2 mT in-plane to 11.2 mT out-of-plane.

4.2 NLC1

This sample is layered like NGO|LSMO(13nm)|Cu(10nm). The purpose of this sample was to see how the parameters of LSMO, in particular the parameters of sample NL1, would change if a layer of Cu is sputtered on it. The Cu layer was grown directly after the just grown LSMO had been cooled down, at a temperature of 27 °C. No EPR/FMR measurements have been done for this sample.

4.2.1 Topography

To see whether or not the surface of the Cu layer was uniform, the topography was imaged. This is shown, along with a profile, in Fig. 4.2.1.
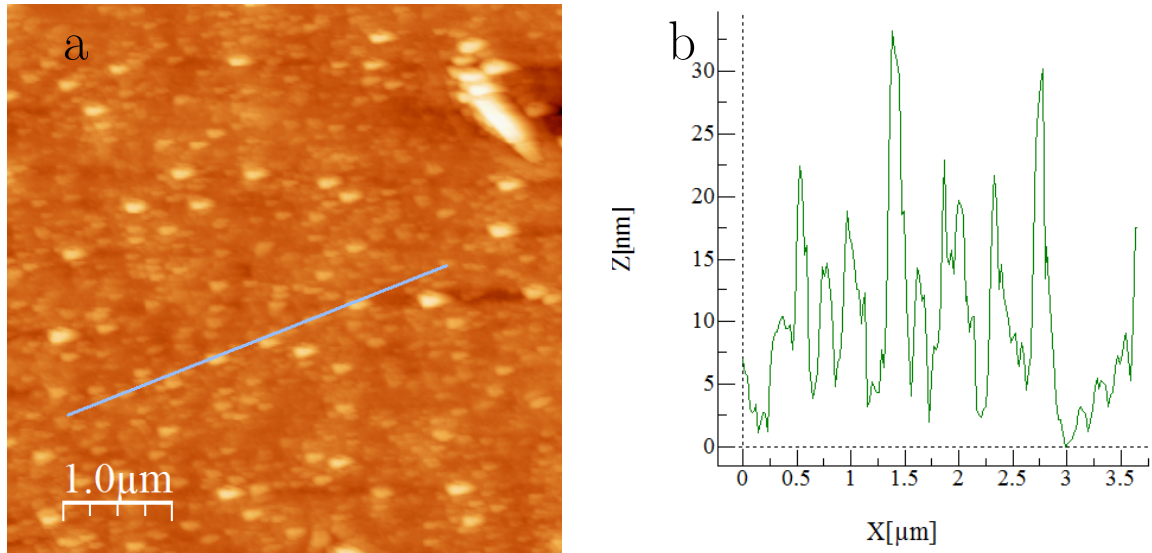
Figure 4.2.1: (a)The topography of NLC1. (b) The profile along the line in (a). The profile shows that there are holes in the Cu layer, reaching into the $La_{0.7}Sr_{0.3}MnO_3$ layer. The RMS roughness is 7.5 nm.

The image shows that there are deep holes in both the Cu and LSMO layers.

4.2.2 X-ray Diffraction measurement

After the surface was imaged, and showed signs that the LSMO layer may have been damaged, along with the ferromagnetism, an X-ray diffraction measurement was done, to see whether the LSMO still had the perovskite structure. The X-ray diffraction measurement is shown in Fig. 4.2.2.
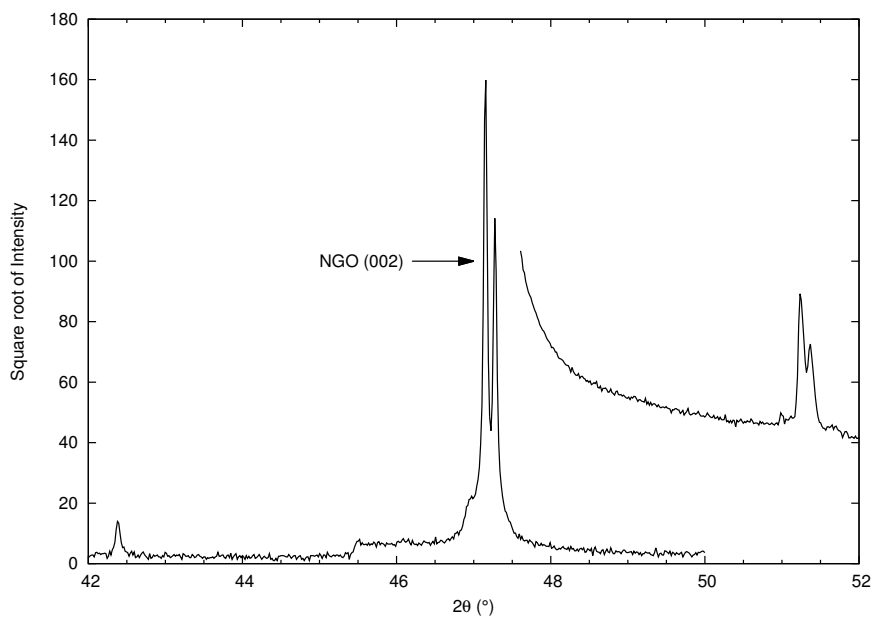

Figure 4.2.2: X-Ray diffraction of NLC1. It consists of two measurements. The bottom left measurement was done with a Cu filter, at 20 mA. The top-right at 30 mA.

4.2.3 Magnetisation measurements

Finally, to check the actual ferromagnetism itself, the magnetisation of the sample as a function of the external field was measured, at a temperature of 15 K. This is shown in Fig. 4.2.3.
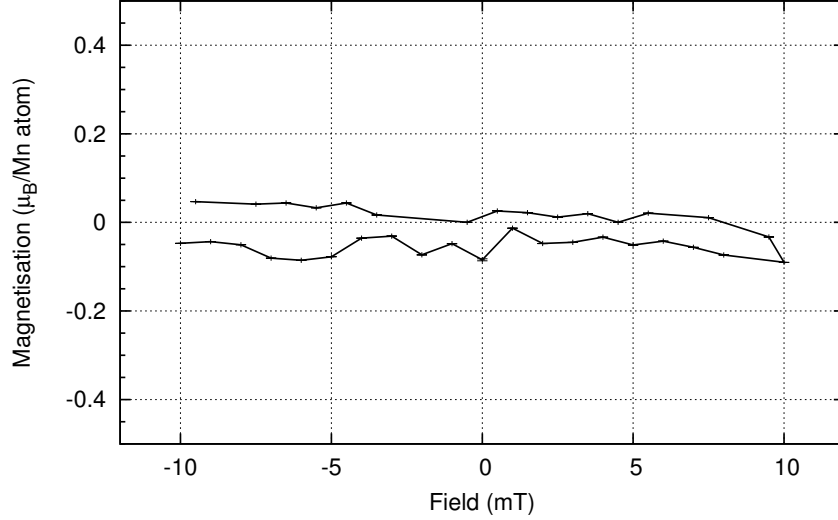

Figure 4.2.3: The magnetisation of NLC1-m1 as a function of the external field. This measurement was done at a temperature of 15 K. No saturation magnetisation can be determined.

No hysteresis loop can be found in this graph.

4.2.4 Discussion of NLC1

We had not been able to deposit a uniform Cu layer on top of the LSMO without changing the system as seen from M_s. The sample has a high RMS roughness, of 7.5 nm, and the Cu atoms seem to cluster.

Since the next sample, LC1, shows that Cu grows amorphous at 100 °C, it would seem that it should also grow amorphous at 27 °C. Therefore, it could be that the LSMO itself was not grown uniformly.

4.3 LC1

This sample is layered as LAO|Cu(10nm).

Because it may be that the Cu layer on the NLC1 sample has severely diminished the ferromagnetism, this is a check to see with what growth parameters a smooth Cu layer can be grown. It was found, from [20], that Cu grows amorphous on LAO at a temperature of 100 °C. The topography is shown in Fig. 4.3.1. The growth parameters themselves can be found in Appendix B.
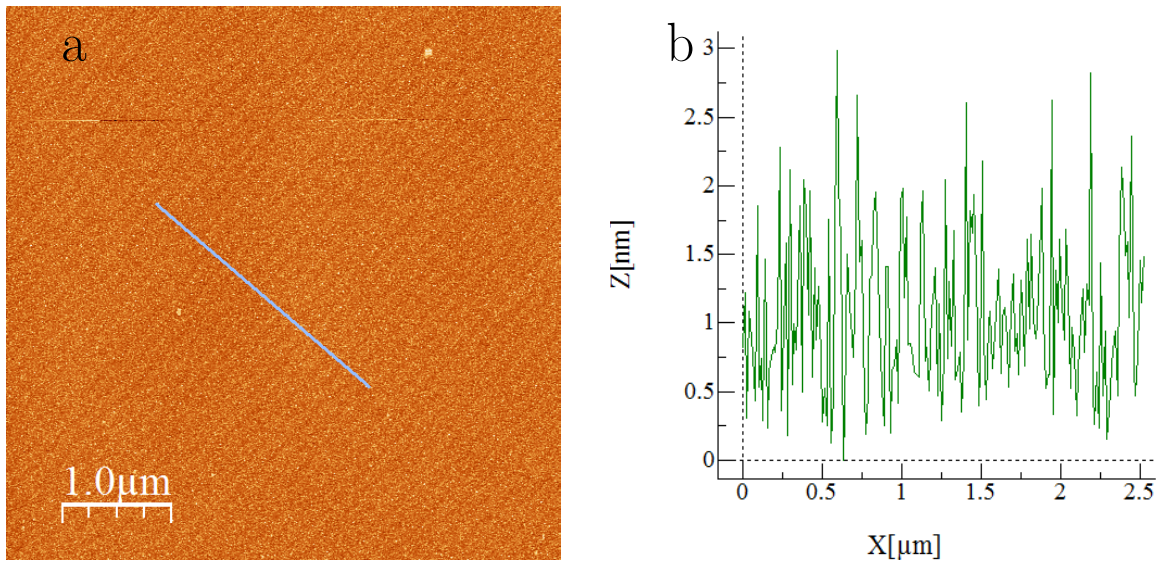
Figure 4.3.1: (a) The topography of LC1. (b) The profile along the line in (a). The topography of the underlying LAO is visible on the Cu layer, indicating that the Cu layer is very smooth. The RMS roughness is 0.57 nm.

The resulting layer of Cu is smooth and the structure of the underlying LAO is visible.

4.4   NLC2

This sample is NL1 on which a Cu layer was deposited, at 100 °C. This depositing was done more than a month later. The purpose of this was to check if a Cu layer could also grow uniformly on a layer of LSMO, and not just LAO. The magnetisation as a function of the external magnetic field and the angular dependence of the linewidth are also measured and compared with those measurements of sample NL1.

4.4.1   Topography

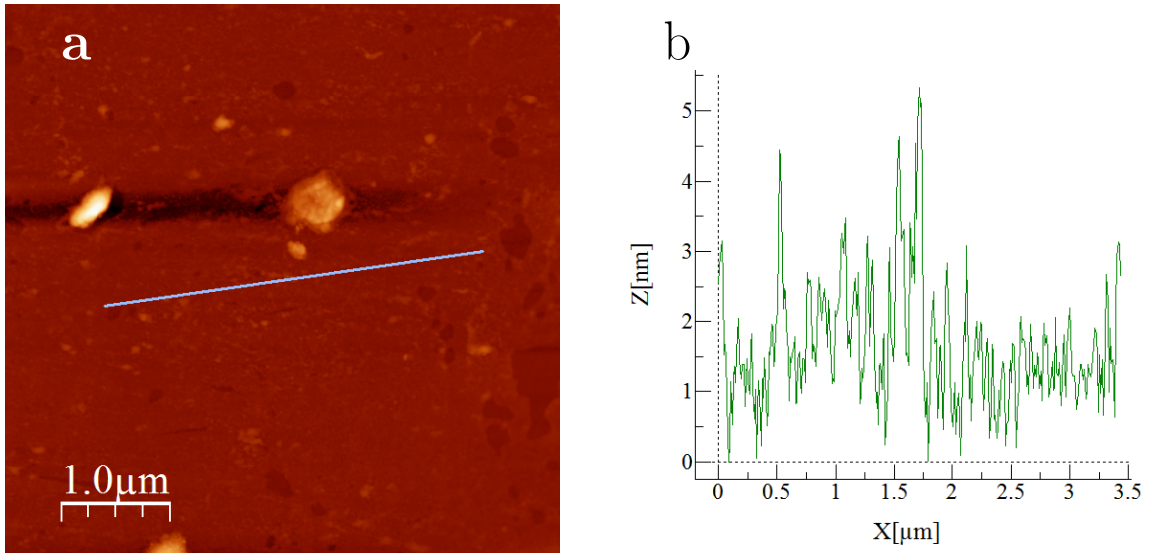The topography is shown in Fig. 4.4.1. Fig. 4.4.2 shows a zoomed in portion of a smooth area of Fig. 4.4.1.

21

Figure 4.4.1: (a) The topography of NLC2-6(m). (b) The profile along the line in (a). The RMS roughness is 2.2 nm.
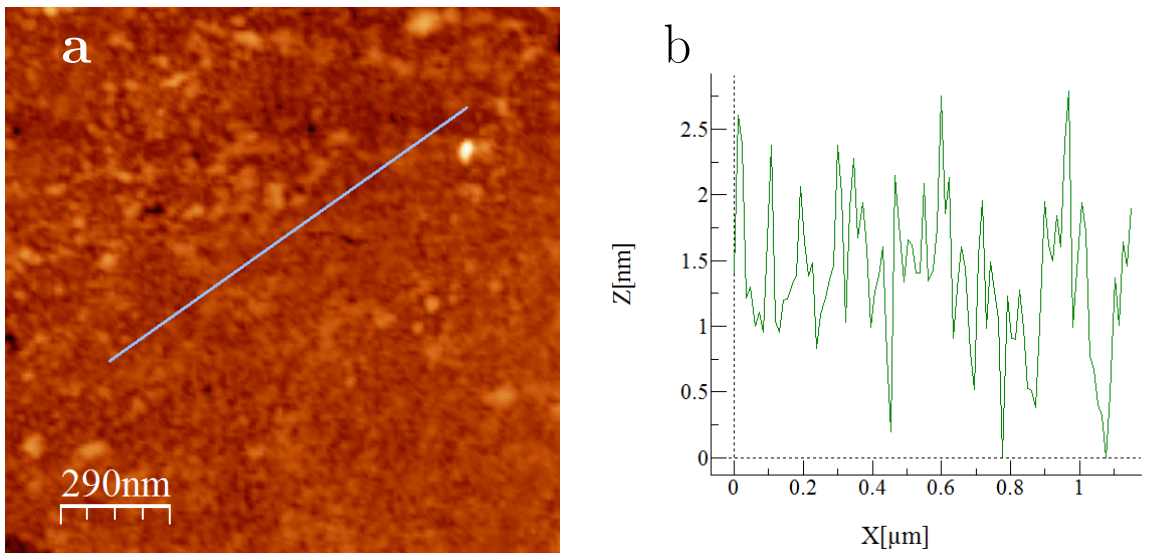

Figure 4.4.2: (a) The topography of NLC2-6(m). (b) The profile along the line in (a). This shows that the surface is very smooth locally.

4.4.2   Magnetisation measurements

The topography shows that the Cu layer is quite smooth, however, it doesn't give much information about the condition of the LSMO layer underneath. To check whether the it was still intact and ferromagnetic, the magnetisation was measured as a function of the external field, at 15 K. The results are shown in Fig. 4.4.3.
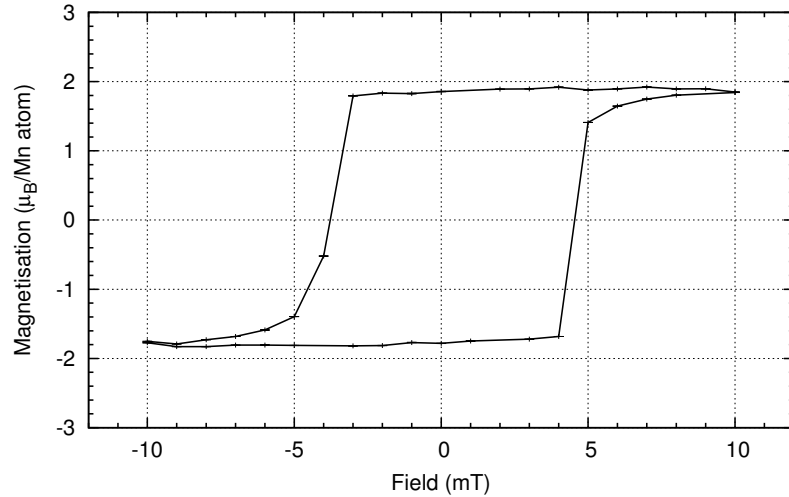
Figure 4.4.3: The magnetisation of NLC2-4(s) as a function of the external field at a temperature of 15 K.

4.4.3 FMR measurements

The angular dependence of linewidth was measured for NLC2-6(m), at room temperature. This is shown in Fig. 4.4.4.
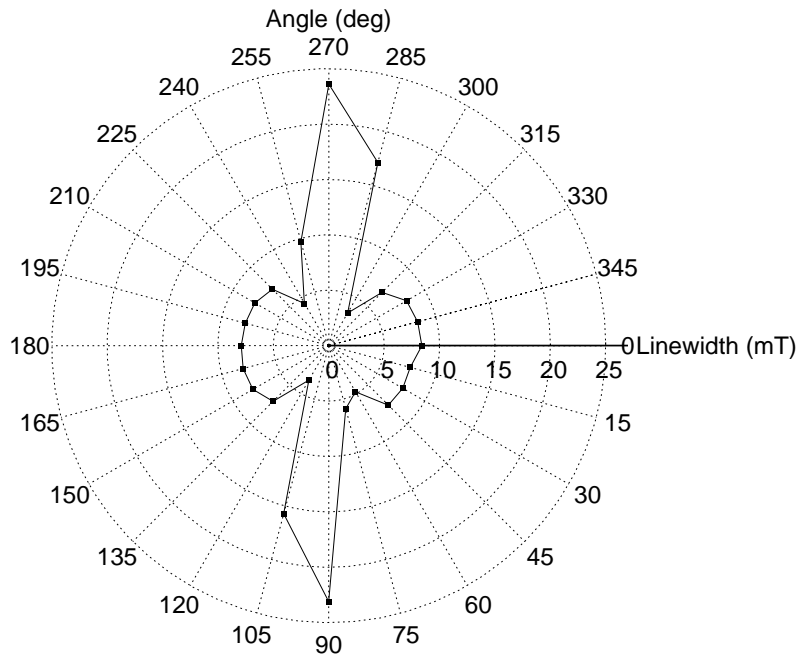

Figure 4.4.4: The angular dependence of the linewidth of NLC2-6(m) at a temperature of 293 K.

4.4.4 Discussion of NLC2

The AFM images show that the surface is reasonably smooth, with an RMS roughness of 2.2 nm. M_s is shown to be 1.9 μ_B/Mn atom, at a temperature of 15 K. The measurement of M_s of NL1 was done at a temperature of 10 K, so it might not have changed after sputtering Cu on the sample.

The linewidth varies from 8 mT in-plane to 23 mT out-of-plane, meaning that the in-plane linewidth has not significantly changed, but the out-of-plane linewidth has more than doubled. Maybe the LSMO layer is not uniform at the edges anymore, causing this behaviour.

4.5 NLC3

This sample is layered as NGO|LSMO(10nm)|Cu(10nm). It is the attempt to grow a uniform layer of Cu on top of a uniform layer of LSMO, with a better interface.

4.5.1 Topography

The topography and the profile of NLC3, as measured by AFM, is shown in Fig. 4.5.1.
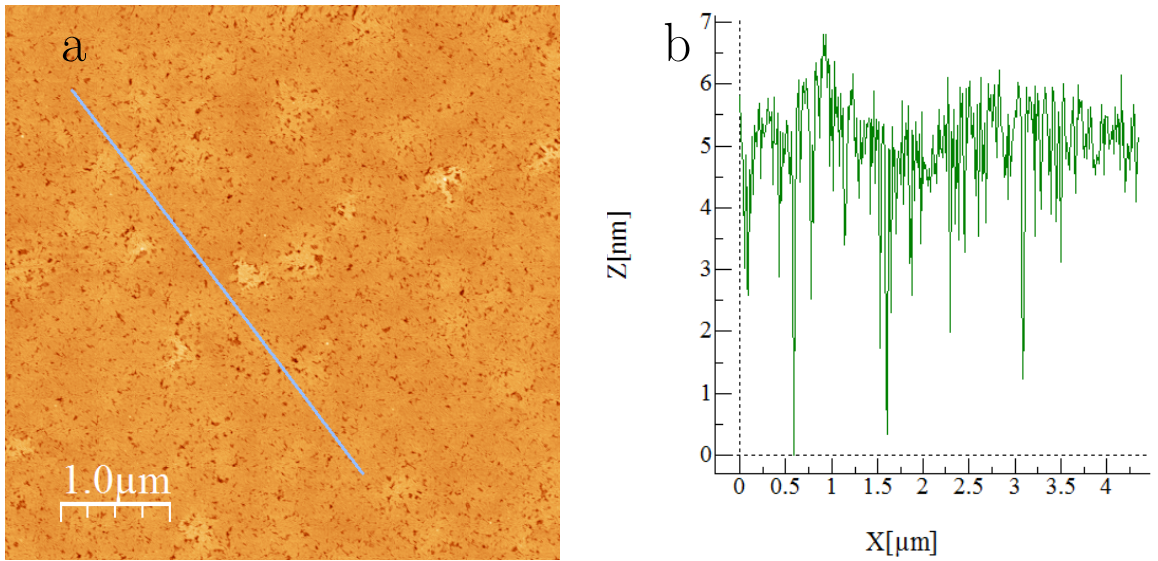

Figure 4.5.1: (a) Topography of NLC3. (b) The profile along the line in (a). This shows that while there are holes in the Cu layer, there are no visible holes in the $La_{0.7}Sr_{0.3}MnO_3$ layer. The RMS roughness is 1.08 nm.

4.5.2 X-Ray diffraction measurement

The X-ray diffraction measurements of NLC3 is shown in Fig. 4.5.2 and Fig. 4.5.3.
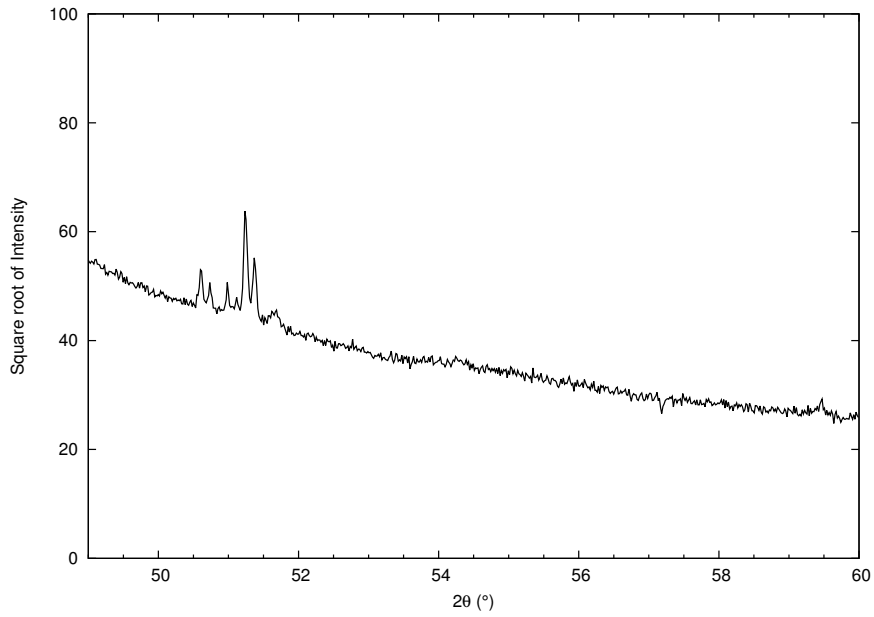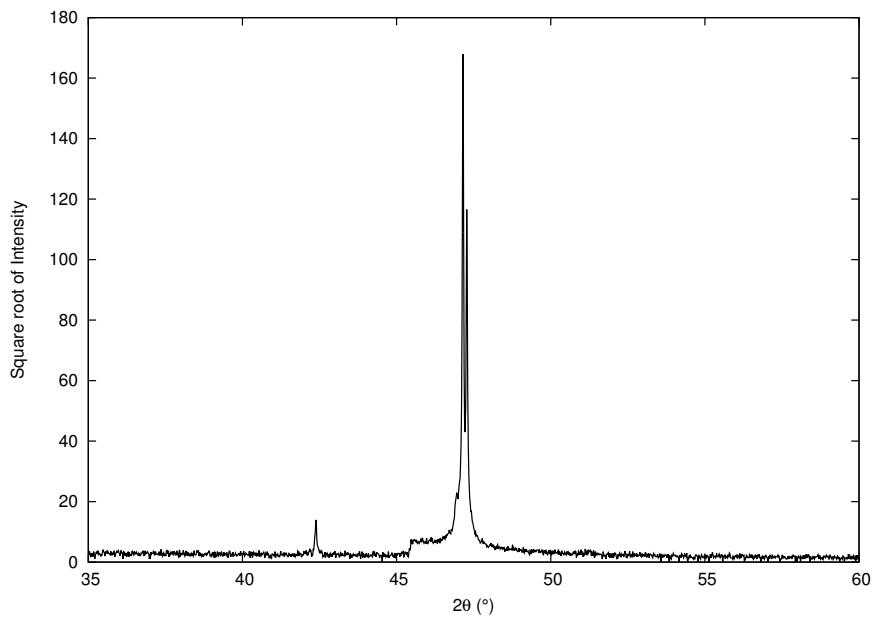
Figure 4.5.2: X-Ray diffraction of NLC3.

Figure 4.5.3: X-Ray diffraction of NLC3 at 20 mA with a Cu filter. No Cu peak can be seen, confirming that the Cu layer is amorphous.

4.5.3 Magnetisation measurements

The magnetisation as a function of the external field was measured at 15 K. The result is shown in Fig. 4.5.4.
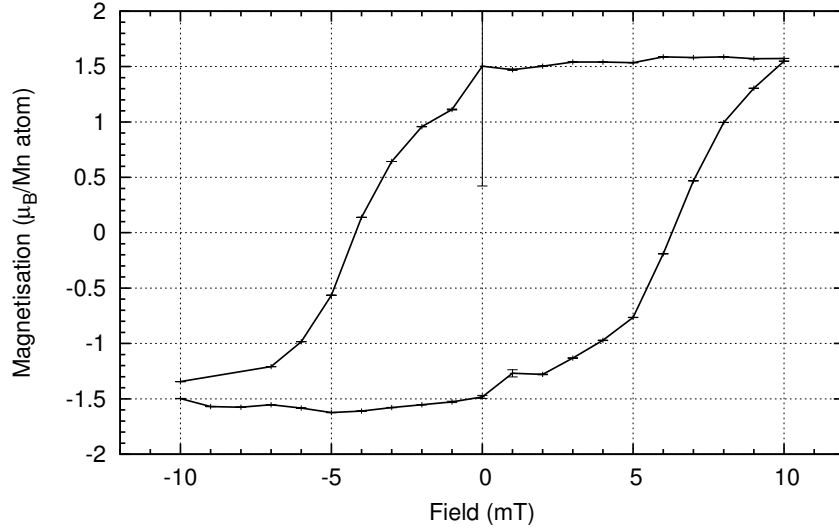
Figure 4.5.4: Magnetisation vs. external field of NLC3-m at a temperature of 15 K.

4.5.4 FMR measurements

The angular dependence of linewidth of NLC3 was measured and is shown in Fig. 4.5.5.

Figure 4.5.5: Angular dependence of linewidth of NLC3-m at a temperature of 293 K.

4.5.5 Discussion of NLC3

The surface of this sample has an RMS roughness of 1.08 nm. The M_s was measured to be 1.5 μ_B/Mn atom. Interestingly, the linewidth has increased significantly, ranging from 28 mT in-plane, to 38 mT out-of-plane. It is not known why this happens. One explanation is that the Cu sputtered on had another material in it, perhaps even magnetic.

4.6 NLCP1

This sample is layered as NGO|LSMO(10nm)|Cu(5nm)|Pt(15nm).

To test for the presence of spin pumping, half of the Cu layer of NLC3 was etched off, and a 15 nm layer of Pt was deposited on the sample. This etching was done at room temperature, using an Argon flow of 50 sccm and 75 W power. The Pt layer was grown at room temperature, as well.

4.6.1 Magnetisation measurements

To check whether or not the act of depositing Pt on the sample has diminished the Curie temperature, the magnetisation as a function of the temperature was measured for this sample. The result is shown in Fig. 4.6.1.

Figure 4.6.1: Magnetisation as a function of temperature of NLCP1-m in an external field of 0.6 mT. The T_C is still 320 K.

To compare with the sample without the Pt layer on it, Fig. 4.6.2 shows the magnetisation as a function of the extenal magnetic field.
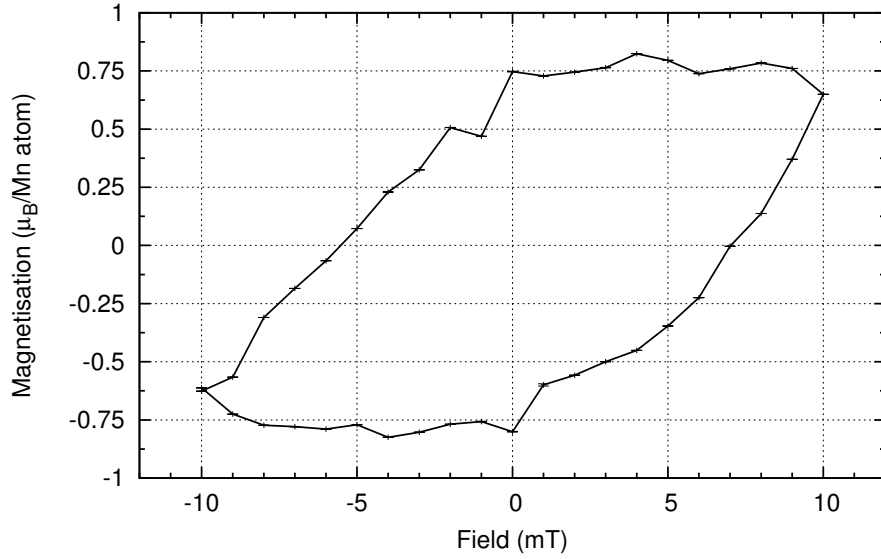
Figure 4.6.2: Magnetisation as a function of the external magnetic field of NLCP1-m at a temperature of 15 K.

4.6.2 FMR measurements

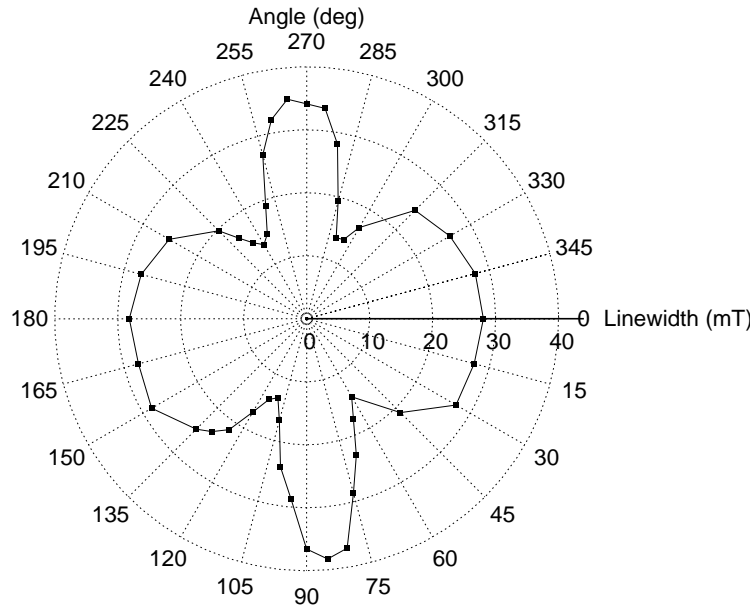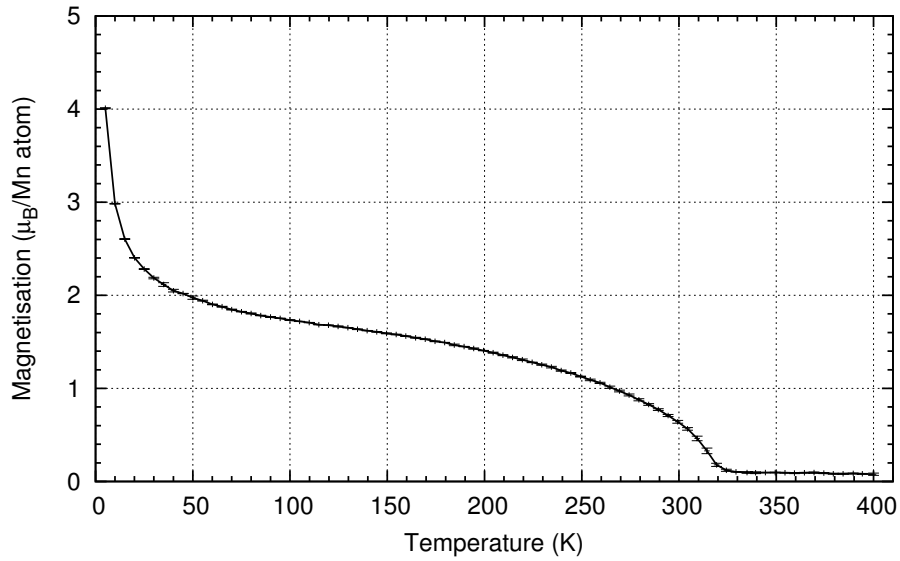The angular dependence of linewidth of NLCP1 is shown in Fig. 4.6.3. The linewidth was measured from 0° to 180°, and the measured values were then mirrored over to the 180-360° domain.
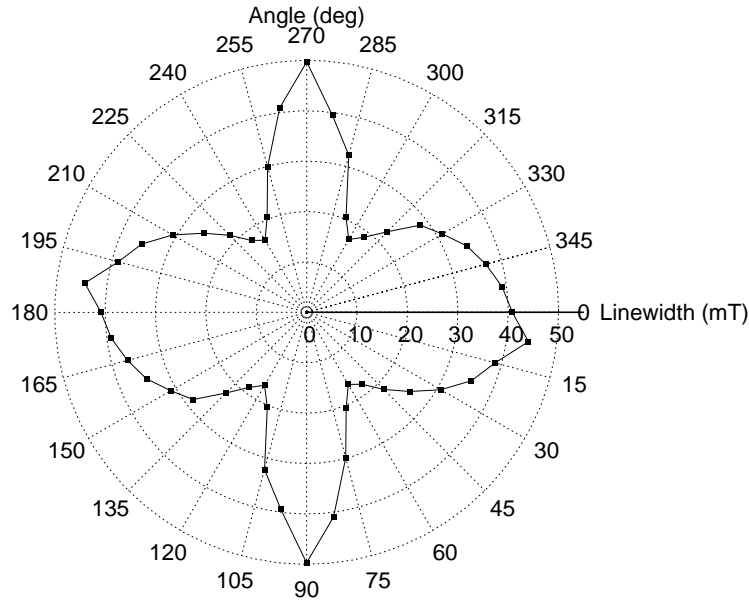
Figure 4.6.3: Angular dependence of linewidth of NLCP1-m, at a temperature of 293 K.

4.6.3 Discussion of NLCP1

It was found that the T_C remains 320 K after etching away Cu and sputtering Pt on the sample. The saturation magnetisation M_s has been halved, with respect to the sample without a layer of Pt. The linewidth seems to have increased, from 45 mT in-plane, to

50 mT out-of-plane. Spin Hall Effect measurements of this sample have shown no sign of a voltage induced by a spin current.

4.7 LP1

This sample is layered as LAO|Pt(11.5nm).

Since it is not known whether the layer of Pt of the previous sample, NLCP1, was uniform, plus the fact that the interfaces between adjacent layers could be bad, another test sample was made. This time to check how a uniform, amorphous Pt layer can be grown. The Pt layer of this sample is grown at a temperature of 400 °C. This temperature was taken, because of a paper which showed that Pt could be grown amorphous on perovskite substrates at 400 °C[20].

4.7.1 Topography

Fig. 4.7.1 shows the topography of LP1.
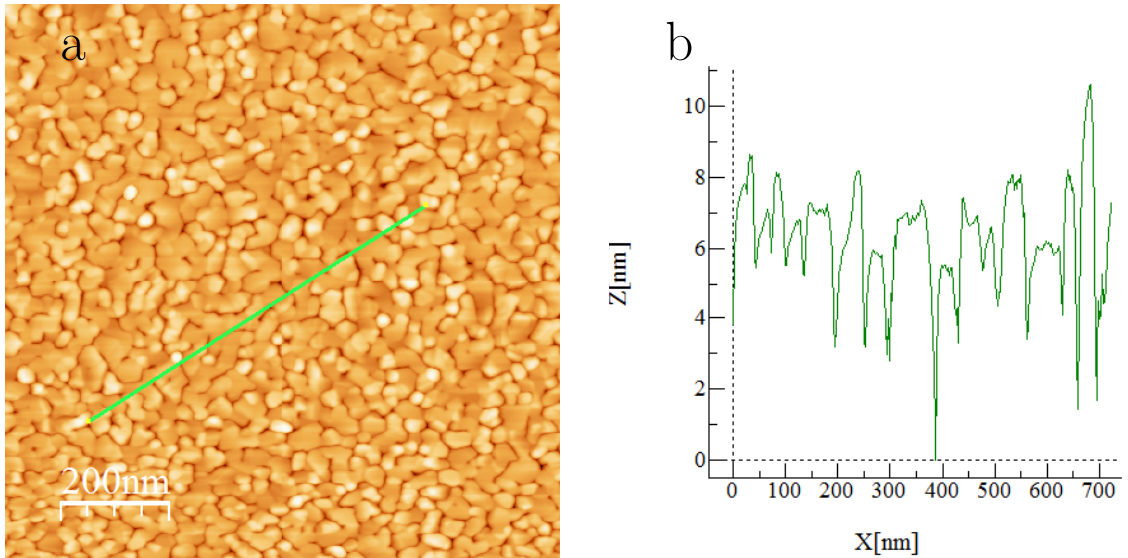
Figure 4.7.1: (a) AFM image of LP1. (b) The profile along the line in (a). This shows that, at 400 °C, the platinum formed structures on the LAO, and is thus not amorphous. The RMS roughness is 1.52 nm.

4.7.2 X-ray Diffraction

The XRD measurement in Fig. 4.7.2 shows a distinct peak of Pt, indicating that the Pt is structured, and not amorphous.

Figure 4.7.2: XRD of LP1. A filter has been used to diminish the Pt peaks. The thinner peaks are all from the LAO substrate.

4.8   LP2

This sample is layered as LAO|Pt(?nm). The thickness of the Pt layer is not known, but it was grown in the same system and for the same amount of time as the LP1 sample.

The temperature of 400 °C seems too high for growing Pt on LAO. The Pt layer of the next sample is therefore grown at 250 °C.

4.8.1   Topography

The topography is shown in Fig. 4.8.1 and Fig. 4.8.2 .
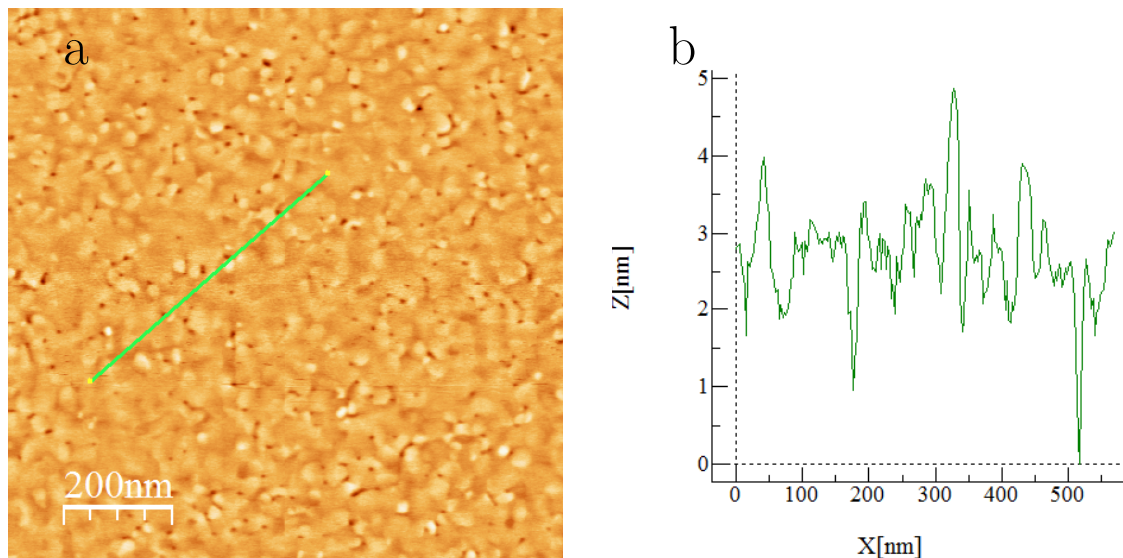
Figure 4.8.1: (a) AFM image of LP2. (b) The profile along the line in (a). The RMS roughness is 0.70 nm.

Zooming out, it is possible to see the underlying structure of the LAO.
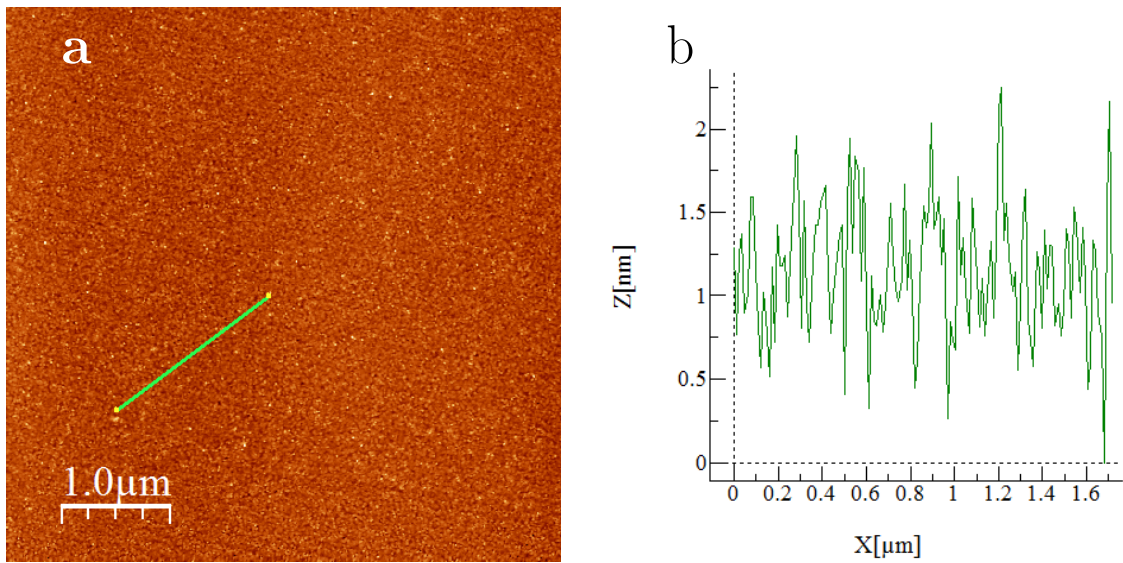
Figure 4.8.2: (a) AFM image of LP2. (b) The profile along the line in (a).

4.8.2 X-ray Diffraction

The X-Ray diffraction measurement in Fig. 4.8.3 still shows peaks of Pt, indicating that the Pt is structured in the (111) direction.

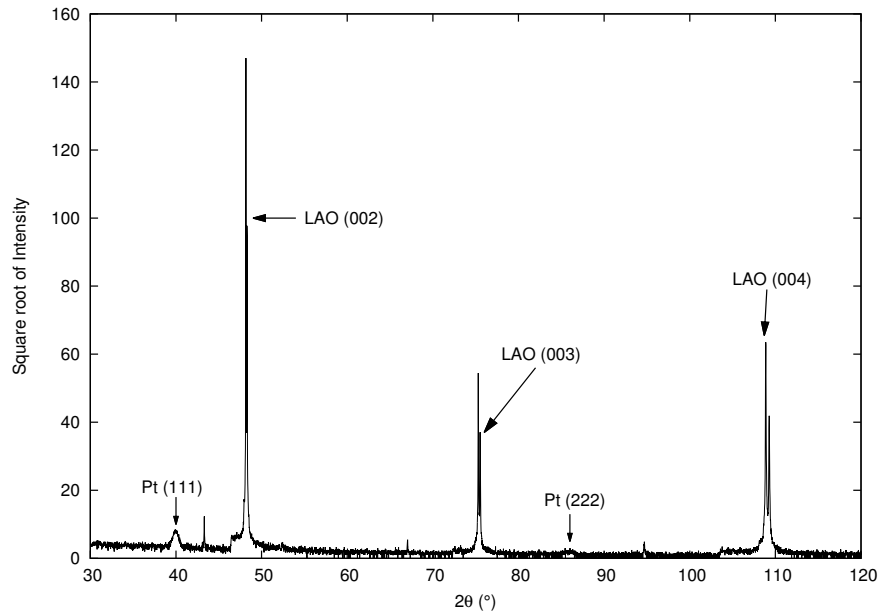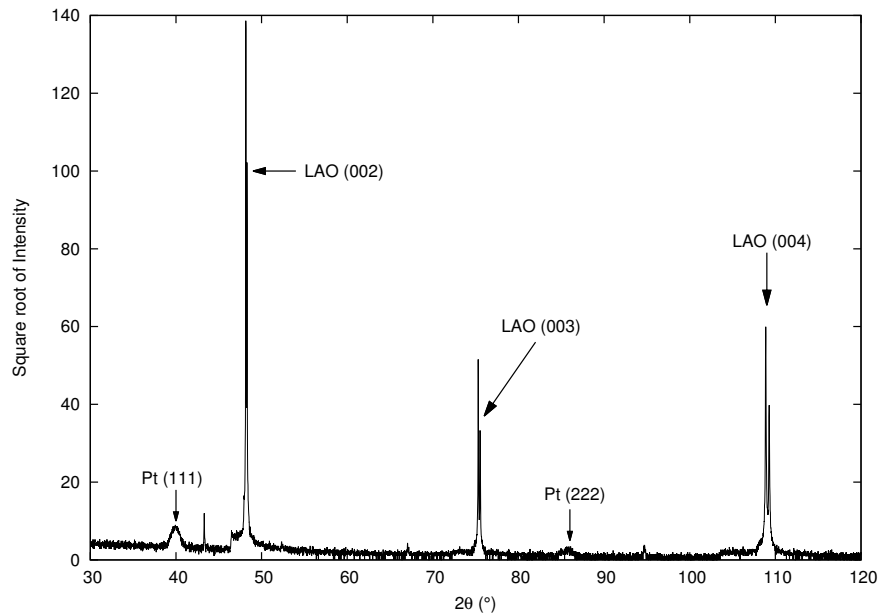**Figure 4.8.3:** XRD of LP2. A filter has been used to diminish the Pt peaks. The thinner peaks are all from the LAO substrate.

The Pt is taken to be smooth enough, and the following Pt layers will be grown at 250 °C.

4.9   NLP1

This sample is layered as NGO|LSMO(?nm)|Pt(?nm). Neither the thickness of the LSMO layer, nor the thickness of the Pt layer is known.

   This is the attempt to grow Pt directly on LSMO, for a better interface.

4.9.1   Topography

Fig. 4.9.1 shows the topography of this sample.
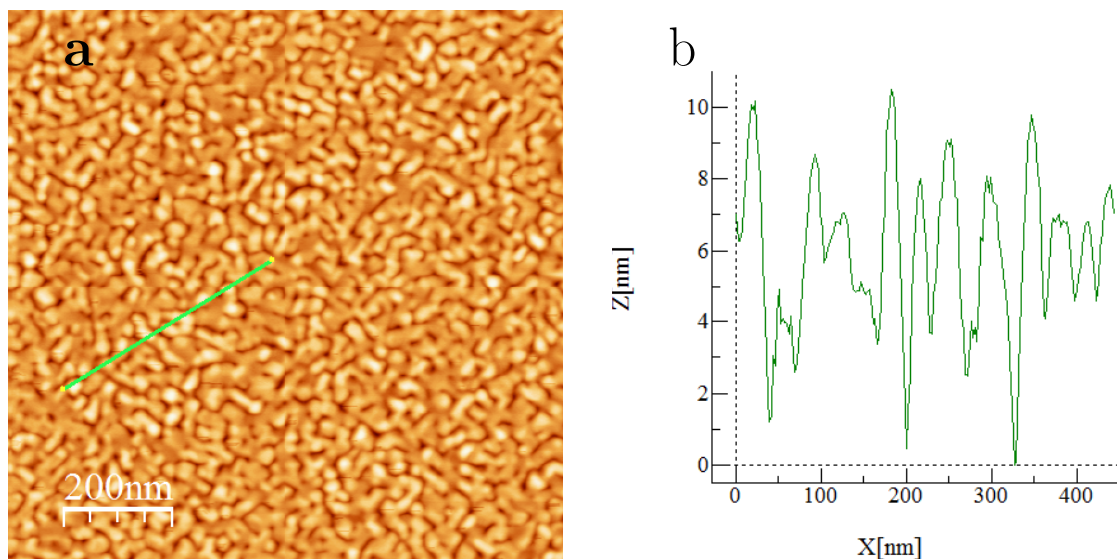
Figure 4.9.1: (a) AFM image of NLP1. (b) The profile along the line in (a).

4.9.2   Magnetisation measurements

The magnetisation was measured both as a function of the temperature and as a function of the external field. This is shown in Fig. 4.9.2 and Fig. 4.9.3, respectively.
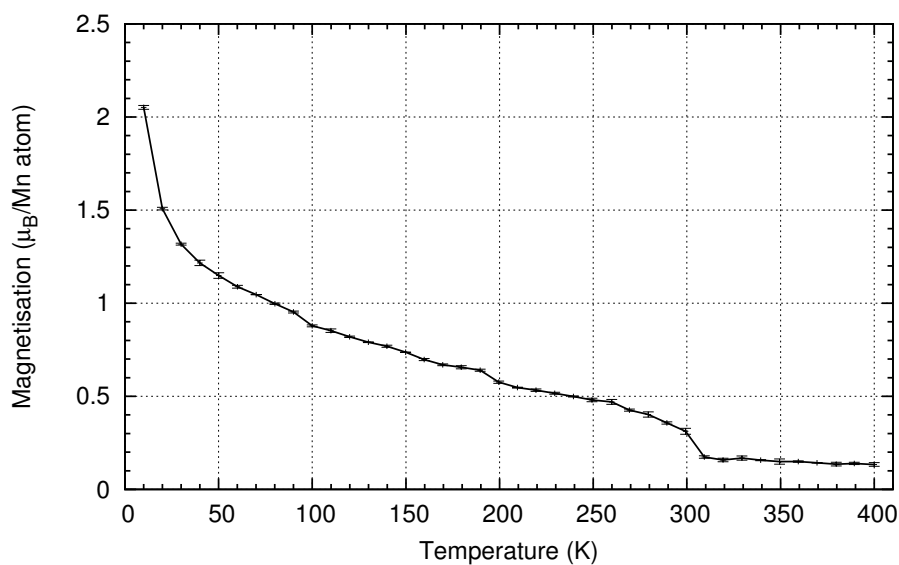
Figure 4.9.2: Magnetisation as a function of temperature of NLP1-m1 in an external field of 0.6 mT. The T_C has diminished to 305 ± 5 K.
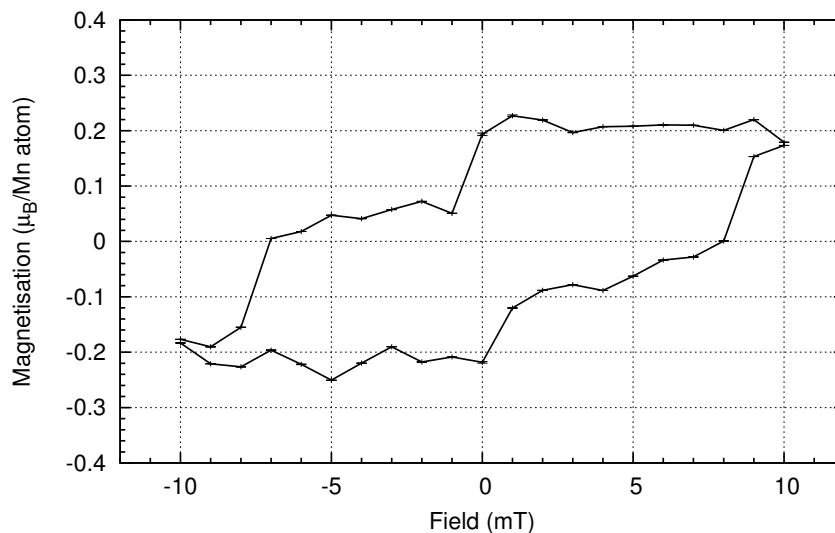
Figure 4.9.3: Magnetisation as a function of external field of NLP1-m1 at a temperature of 15 K. The M_s is 0.2 μ_B/Mn atom.

4.9.3 X-ray diffraction measurements

The X-ray diffraction measurement, shown in Fig. 4.9.4, shows no Pt(111) peaks.
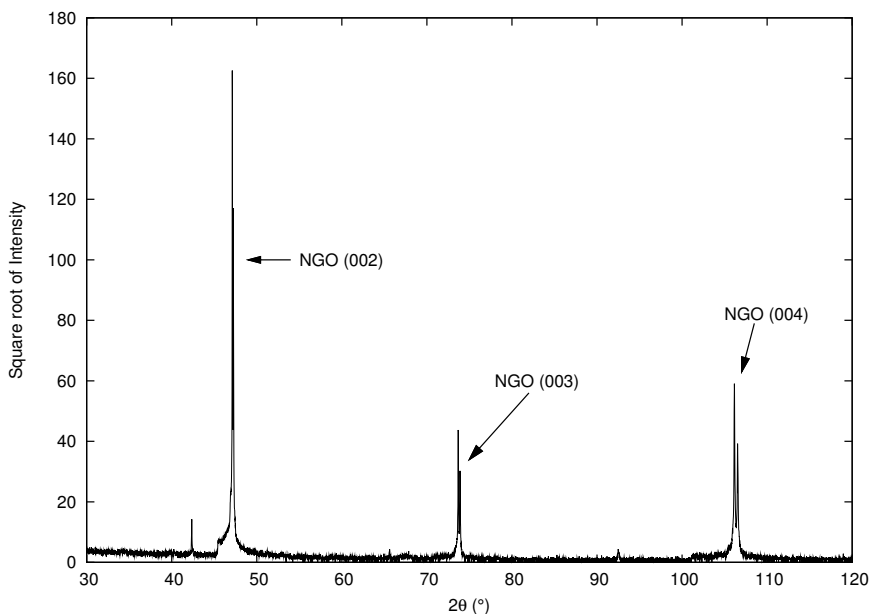
Figure 4.9.4: X-Ray diffraction of NLP-m1, with a Cu filter. The measured peaks belong to the substrate. No Pt(111) peaks can be seen.

4.9.4 FMR measurements

Fig. 4.9.5 shows the angular dependence of linewidth. The linewidth was measured from 0° to 180°, and the measured values were then mirrored over to the 180°-360° domain.
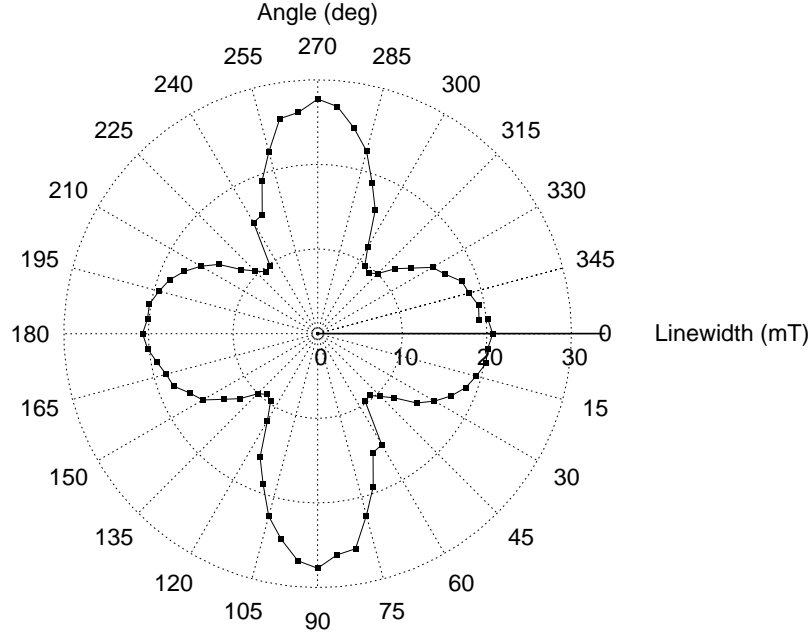
Figure 4.9.5: Angular dependence of linewidth of NLP1-m2 at a temperature of 293 K.

4.9.5 Discussion of NLP1

Interestingly, the AFM image in Fig. 4.9.1 shows a lot of structure in the Pt layer, but the X-ray diffraction measurement, in Fig. 4.9.4, shows no Pt(111) peak at all. It could be that Pt grows differently on LSMO, which may be caused by a different termination of LSMO. This may cause Pt to grow in another direction. The small bump in Fig. 4.9.4 at ~67° could be from Pt(220).

The T_C has diminished to 305 ± 5 K. M_s of this sample is 0.2 μ_B/Mn atom. This is about 10% of NLC2, the sample with just a layer of Cu on it. The growth temperature of Pt is most likely still too high.

The linewidth varies from 20 mT in-plane to 28 mT out-of-plane, which is less broad than the linewidth of sample NLCP1.

Chapter 5

Discussion

In this chapter the measurements will be compared and the results shown in the previous chapter will be discussed.

The goal of this project is to check if it is possible to induce a spin current from LSMO into Pt with spin pumping. To check this, there are a few subgoals to complete. These are:

1. To check if LSMO has FMR using EPR.

2. Growing a smooth layer of Cu on smooth LSMO. The linewidth of the FMR signal must not increase by doing this, as Cu is a bad spin sink. The LSMO must also stay intact, meaning the structure and the magnetisation.

3. Growing a smooth layer of Pt on LSMO. If a spin current is induced, the linewidth of the FMR signal should increase, as Pt is a good spin sink.

4. To check for an inverse spin Hall voltage.

5.1 LSMO

5.1.1 Quality of sample

The surface was imaged to see if the LSMO had been grown uniformly. This was done by AFM and is shown in Fig. 4.1.1. The roughness of the layer was measured to be 0.33 nm, meaning the LSMO layer of this sample is very smooth.

The magnetisation was measured as a function of the temperature and as a function of the external field, to measure the Curie temperature T_C, the coercive field and the saturation magnetisation M_s. The T_C is measured to be 320 K, as shown in Fig. 4.1.2.

In this same image, the signal of the paramagnetic NGO can be seen to follow the $1/T$ dependence of the Curie law. This becomes prominent for $T \leq 50$ K. If $T \geq T_C$, the signal is both from the NGO and the now paramagnetic LSMO.

Fig. 4.1.3 shows the magnetisation along the hard anisotropic axis at 10 K, and shows that the coercive field is 3.9 mT. M_s is shown to be 2.0 μ_B/Mn atom. To arrive at these numbers, the signal of the paramagnetic NGO was subtracted from the measured, total signal.

The measured 2.0 μ_B/Mn atom is just more than half the theoretical value of M_s, which equals 3.5 μ_B/Mn atom. The difference between the theoretical and the measured value could be explained by a few things. One of these is by the inclusion of a dead layer.

A reason for the dead layer could be a loss of Oxygen in the LSMO. Oxygen can leave the structure of the outside layers when the temperature is greater than 400 °C. This loss of Oxygen means that the double exchange mechanism disappears in these layers, causing the LSMO to lose both its ferromagnetic and its half-metallic properties. Since all the LSMO layers are grown at 840 °C, and then cooled in vacuum, there is a chance that some of the Oxygen has left the LSMO before a normal metal is grown on it. Perhaps the LSMO must be cooled in an Oxygen atmosphere.

The thickness of the dead layer can be calculated from the saturation magnetisation. The theoretical value of M_s is 3.5 μ_B/Mn atom. The measured M_s is 2.0 μ_B/Mn atom for the best measurement. The total thickness times the measured M_s divided by the theoretical M_s gives the thickness of the magnetic layer in nm, and so:

$$d_{\text{dead layer}} = d_{\text{total}} \left(1 - \frac{M_{s,\text{measured}}}{M_{s,\text{theoretical}}} \right). \tag{5.1.1}$$

Using Eq. (5.1.1), the thickness of the dead layer is calculated to be 5.57 nm.

The X-ray diffraction measurements do not show a visible LSMO peak. this could be due to the low lattice mismatch between LSMO and NGO; the NGO(002) peak is greater than the LSMO(002) peak, and overlaps with it.

5.1.2 FMR signal

A few of the measured FMR spectra are shown in Fig. 4.1.5. At some angles, there seems to be an extra resonance, most likely caused by some inhomogeneities in the LSMO film. Fig. 4.1.6 shows the angular dependence of linewidth, the measured linewidth as a function of the out of plane angle of the external magnetic field. The magnetic anisotropy can be seen in this figure, however, due to the lack of a goniometer, the graph is not symmetrical.

The shape of the anisotropy could be explained by strain caused by the external magnetic field of the EPR set-up. The unit cells of LSMO on orthorhombic (001) NGO are oriented sideways to the external field, shown in Fig. 5.1.1.
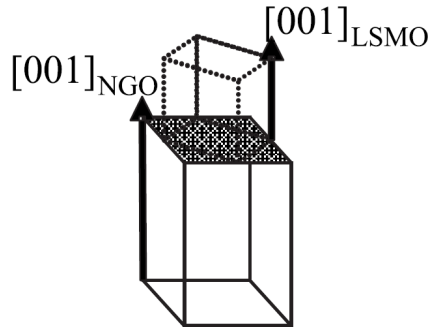
Figure 5.1.1: LSMO(001) grown on orthorhombic NGO(001) is oriented sideways. From [7].

If $\theta_H = 0$, this could cause some tensile strain and a lot of shear on the unit cell, as shown in Fig. 5.1.2. When the sample is rotated by 55°, the shear is mostly gone, and tensile strain in the $[\bar{1}11]$ direction remains. When the sample is rotated by 90°, there is only tensile stain in the [001] direction, which, most likely, costs the least amount of energy.

From the final sample, NLP, it can be seen that the linewidth is the smallest at $\theta_H \approx 55°$. This occurs when the external field is along the diagonal of the unit cell of LSMO. The unit cell is cubic, therefore $\sin(\theta_H + 90°) = \cos\theta_H = \frac{1}{\sqrt{3}} \Rightarrow \theta_H = 54.74°$.
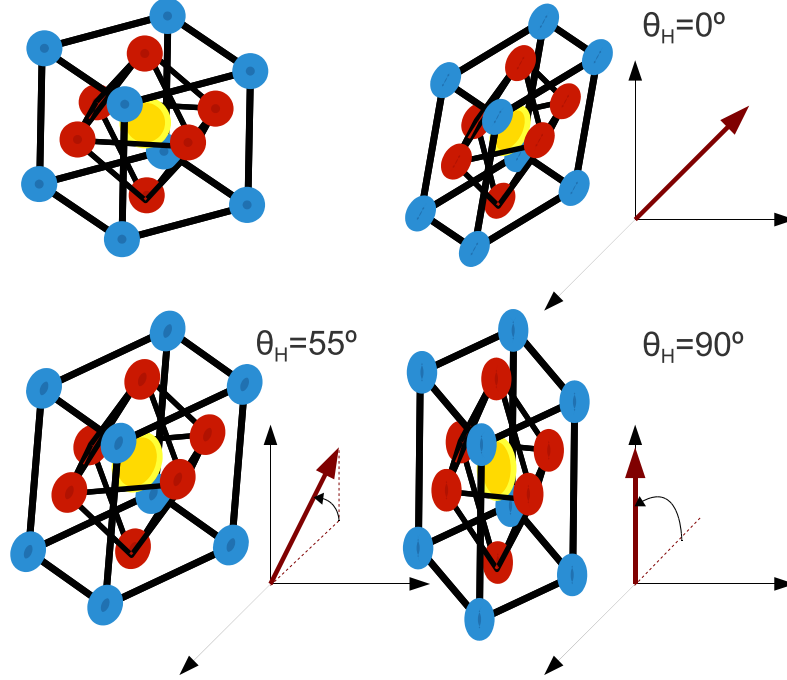
Figure 5.1.2: LSMO unit cell deformation caused by external field as a possible cause of linewidth change. The top left shows a unit cell without an external field.

To get the effective g-factor of 13 nm thick LSMO, the resonance field as a function of the out of plane angle of the external magnetic field was also measured, as shown in Fig. 4.1.7. From this, g_{eff} is calculated to be 1.915. This is calculated by using g_{eff} as a plotting parameter in a Matlab program. The fitted curve is shown in Fig. 5.1.3. By using this measurement, the effective magnetisation M_{eff} can also be calculated in the same way. It is found that M_{eff} is 23.9 mT.
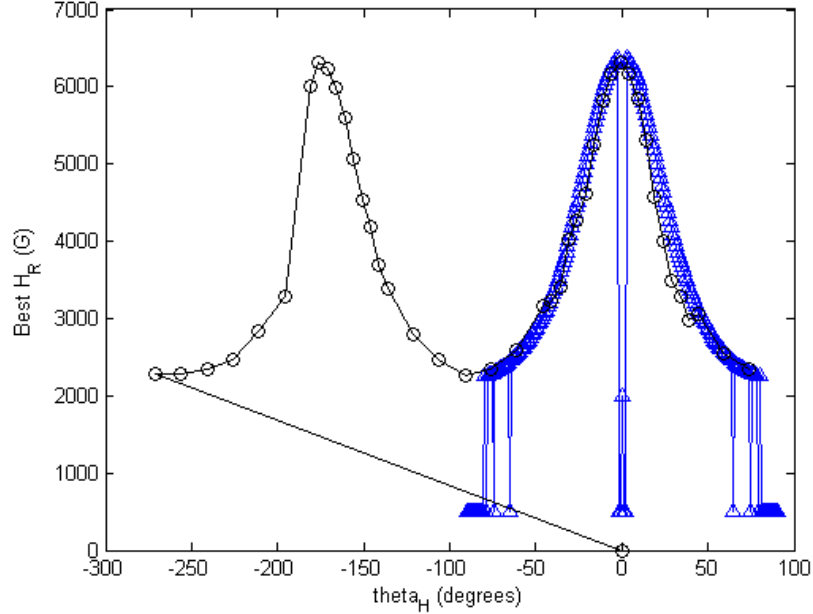
Figure 5.1.3: Fit of the angular dependence of H_r of NL1.

It seems that it is possible to get an FMR signal from LSMO, despite the fact that it is a half-metal.

5.2 Cu on LSMO

5.2.1 Quality of NLC1

The second subgoal was to grow a smooth layer of Cu on smooth LSMO. This proved to be more difficult than first imagined. This is because of the fact that metals grow differently on perovskite structures. They form structures easily and can diffuse into the LSMO, effectively destroying the magnetisation.

The second sample, NLC1, shows that this is possible. For this sample, the Cu layer was grown at room temperature. The surface was imaged using AFM, and is shown in Fig. 4.2.1. It shows that the surface of the Cu layer is very rough, and that there are deep holes in the sample. These holes even go through the LSMO layer, all the way to the substrate.

To confirm that the sample has lost its ferromagnetic property, the magnetisation was measured as a function of the external field. Fig. 4.2.3 shows this result. No hysteris loop can be seen, meaning that the magnetisation has indeed disappeared. A temperature of 15 K was chosen for this measurement because of the paramagnetic NGO and its $1/T$ dependence makes it harder to extract the saturation magnetisation at lower temperatures.

5.2.2 LC1

The next step was to grow a smooth layer of Cu on LSMO, while retaining the magnetisation. In [20] it was found that, if the Cu is grown at 100 °C, the Cu will at least be smooth. This was tested by growing a 10 nm thick Cu layer on LAO (001), of which the surface is shown in 4.3.1. The RMS roughness of this sample is 0.57 nm. The underlying structure of the LAO is visible, meaning the Cu is smooth. Unfortunately, no X-ray

diffraction measurement was done on this sample, so it is not known whether or not the Cu is amorphous or has structure.

5.2.3 NLC2

Quality of sample

To see if the sputtering of Cu on LSMO at any temperature would not destroy the magnetisation, a layer of Cu was grown at $T = 100°$C on an old sample of NL1.While the Cu layer is not so smooth —the RMS roughness is ~ 2.2 nm— as can be seen in Fig. 4.4.1, the magnetisation is diminished only slightly, as Fig. 4.4.3, compared to Fig. 4.1.3, shows.

FMR signal

Since Cu is a bad spin sink, the linewidth should not increase when a layer of Cu is grown on the sample. However, Fig. 4.4.4 does show a small increase of linewidth at the thick "lobes" and a big increase in linewidth at the thinner lobes. This asymmetric increase of linewidth could be due to dirt on the interface between the Cu and the LSMO layer, since the Cu layer was sputtered on the LSMO more than a month later.

5.2.4 NLC3

Quality of sample

The next step is to increase the quality of the interface between LSMO and Cu. This is done by growing Cu on a newly grown LSMO layer in the same system, without taking the sample out first. Fig. 4.5.1 shows that the Cu is smooth, with an RMS roughness of 1.08 nm.

The X-ray diffraction measurement in Fig. 4.5.2 shows peaks, presumably originating from imperfections in the substrate.

The measured M_s for this sample is, as shown in Fig. 4.5.4, around 1.5 μ_B/Mn atom. Presumably, the dead layer is thicker for this sample. Using Eq. (5.1.1), it is calculated that $d_{\text{dead layer}} = 5.71$ nm.

FMR signal

The FMR measurements show that there is an increase in linewidth, as shown in Fig. 5.2.1. It is not known why this happens. Perhaps the Cu is contaminated with another (possibly magnetic) metal.
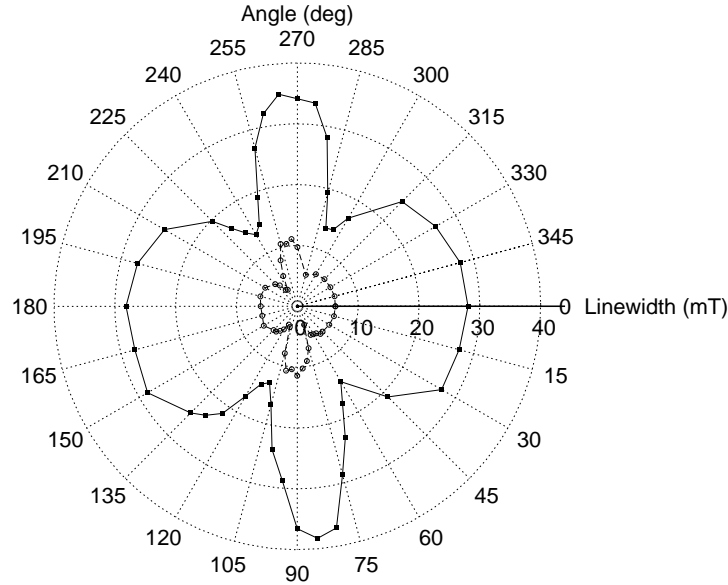
Figure 5.2.1: Comparison of the linewidth of NL1 (open circles) and NLC3 (closed squares).

5.3 Pt on LSMO

5.3.1 NLCP1

Growing Pt on LSMO should increase the linewidth of the FMR signal, assuming a spin current is induced. This is first checked by growing a layer of Pt on the previous sample. 5 nm of Cu is etched off, and a 15 nm layer of Pt is then grown on that, at room temperature. This may cause a bad interface, as it is not known how the surface of the etched Cu looks.

Quality of sample

The magnetisation as a function of temperature was measured to see whether the T_C was diminished. This is shown by Fig. 4.6.1. It shows that the T_C is still 320 K. The magnetisation was also measured as a function of the external field, as shown in Fig. 4.6.2. The M_s has decreased to half the original value, now at 0.75 μ_B/Mn atom, which shows that the LSMO layer has been damaged, by either the Argon atoms from the etching of the Cu layer, or the Pt atoms.

FMR signal

The FMR spectrum in Fig. 4.6.3 shows a slight increase in linewidth. A comparison of this sample with the sample without the Pt layer can be seen in Fig. 5.3.1.

Figure 5.3.1: The angular dependence of the linewidth of NLC3-m and NLCP1-m compared.

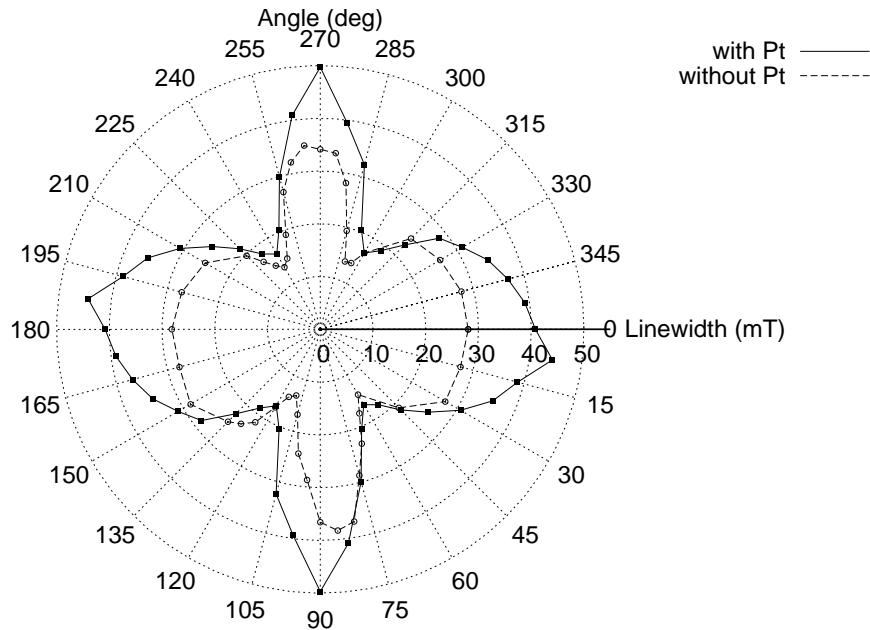The linewidth has increased slightly, but not enough to conclude that spin pumping is the cause. The Pt could have slighty changed the structure of the LSMO, changing the intrinsic damping. Inverse spin Hall voltage measurements show that no spin current was induced.

5.3.2 LP1 and LP2

To grow amorphous Pt directly on LSMO, or any perovskite structure, the temperature for growing the Pt must be carefully chosen. Fig. 4.7.1 shows the topography for LP1 grown at 400 °C. The RMS roughness is 1.52 nm . The X-ray diffraction measurement in Fig. 4.7.2 shows that the Pt has a lot of structure in the (111) direction.

The growth temperature was assumed to be too high. Therefore, another test sample was made, again Pt on LAO,where the Pt was grown at a temperature of 250 °C.

The topography of this sample, LP2, is shown in Fig. 4.8.1. The RMS roughness is 0.70 nm. When looking at a larger area, like in Fig. 4.8.2, the underlying structure of the LAO is visible. Therefore, the temperature of 250 °C is taken to be low enough, and for the next sample with LSMO and Pt on it, the Pt layer will be grown at 250 °C, despite the X-ray diffraction measurement in Fig. 4.8.3 showing that the Pt layer is structured in the (111) direction.

5.3.3 NLP1

Quality of sample

Growing Pt directly on LSMO gives the advantage of having just one interface that has to be good. However, it is not known how this growing affects the LSMO.

The topography of the sample is shown in Fig. 4.9.1. This looks alot like the Pt on LAO grown at 400 °C. It could be that the underlying LSMO layer itself is not uniform.

Fig. 4.9.2 shows that the T_C of NGO|LSMO(?nm)|Pt(?nm) has dropped to a value between 305 ± 5 K. Fig. 4.9.3 shows that the M_s is only 0.2 μ_B/Mn atom. This was

calculated by assuming that the LSMO layer of this sample is 10 nm. The most likely explanation for the low M_s is that the temperature at which Pt was grown was still too high, and the Pt has somehow diffused into the LSMO.

Again assuming the total thickness is 10 nm, the thickness of the dead layer is calculated to be $d_{\text{dead layer}} = 9.42$ nm.

FMR signal

Fig. 4.9.5 shows the angular dependence of FMR linewidth. Fig. 5.3.2 shows a comparison of the linewidths between the bare LSMO, the LSMO with Cu on it and LSMO with Pt on it. It can be seen that the LSMO with a layer of Pt has a smaller linewidth than the LSMO with Cu. According to [14], the linewidth is also dependent on both M_{eff} and M_s. Since $M_s \approx 0.2$ μ_B/Mn atom, the linewidth is smaller than it could be, and this could explain the observed values.
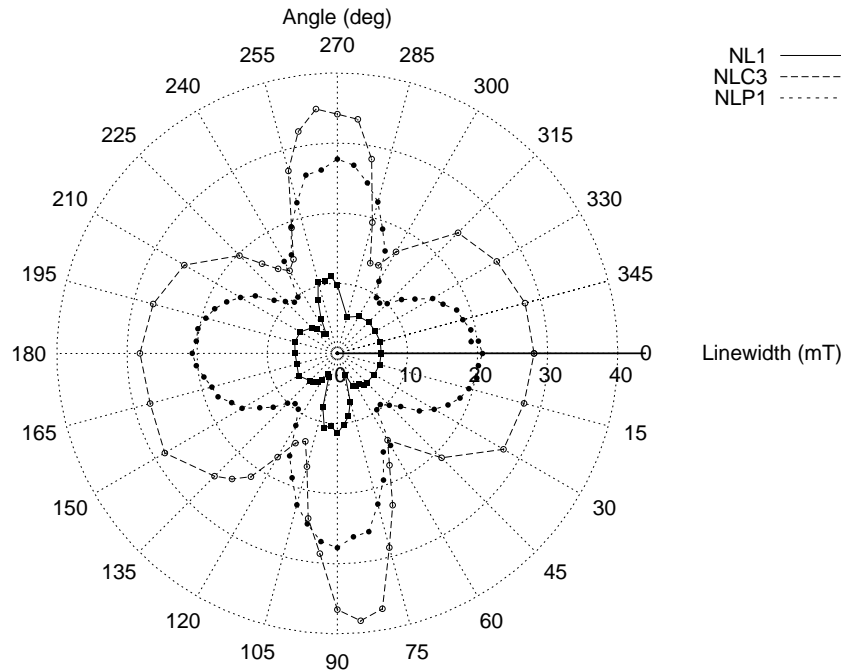

Figure 5.3.2: Comparison of the angular dependence of linewidths of NL1, NLC3, and NLP1.

Inverse Spin Hall Effect

Inverse Spin Hall Effect measurements were also done, on both NLCP1 and NLP1. However, no distinct voltage peak could be found in the noise.

Chapter 6

Conclusions

The Curie temperature of 13 nm thick $La_{0.7}Sr_{0.3}MnO_3$ on (001)-oriented orthorhombic $NdGaO_3$ is shown to be 320 K.

It is possible that oxygen leaves the surface layers of the LSMO while leaving it to cool down in vacuum, causing a dead layer at the surface and diminishing the total magnetisation.

The X-Ray diffraction measurements of LSMO on NGO does not give information about the structure of LSMO. This could be due to the small lattice mismatch between LSMO and NGO, causing the peaks in the XRD spectrum to overlap.

LSMO is shown to have an FMR signal. This FMR signal is strongly dependent on the quality of the LSMO layer, the normal metal grown on top, and the interface between the LSMO and the normal metal layer.

Copper grows amorphous on LSMO at a temperature of 100 °C. If a Cu layer is grown on top of LSMO at room temperature, the Cu may diffuse into the LSMO layer and diminish the magnetisation. It could also be that the LSMO layer in our sample was not uniform to begin with.

A layer of amorphous Cu does not decrease the Curie temperature of LSMO on NGO.

Platinum grows (111)-structured on (001)-oriented LAO at temperatures of both 400 °C and 250 °C. It also grows structured on LSMO at a temperature of 250 °C, which diminishes the magnetisation of the LSMO. However, it is not known whether the Pt is (111)-structured. It is, to us, not known at what temperature Pt grows an amorphous layer on epitaxial (001) LSMO.

The FMR signal of LSMO with Pt on it decreases slighly with respect to LSMO with Cu on it. This could be due to a change in intrinsic damping due to structural changes of the LSMO, or a diminished M_s or M_{eff}.

It is thus far not known whether a spin current can be induced from LSMO into Pt.

Chapter 7

Acknowledgements

Appendix A

Samples

Tables A.1 and A.2 show some basic information about the different LSMO samples.

Sample	name	d_{LSMO}	d_{Cu}	d_{Pt}	Roughn.$_{\text{RMS}}$
NGO|LSMO(13nm)	NL1	13 nm	-	-	0.33 nm
NGO|LSMO(13nm)|Cu(10nm)	NLC1	13 nm	10 nm	-	7.5 nm
LAO|Cu(10nm)	LC1	-	10 nm	-	0.57 nm
NGO|LSMO(13nm)|Cu(10nm)	NLC2	13 nm	10 nm	-	~2.2 nm
NGO|LSMO(10nm)|Cu(10nm)	NLC3	10 nm	10 nm	-	1.08 nm
NGO|LSMO(10nm)|Cu(5nm)|Pt(15nm)	NLCP1	10 nm	5 nm	15 nm	NA
LAO|Pt(11.5nm)	LP1	-	-	11.5	1.52 nm
LAO|Pt(?nm)	LP2	-	-	?	0.53 nm
NGO|LSMO(?nm)|Pt(?nm)	NLP1	?	-	?	1.61 nm

Table A.1: Basic information about all samples.

Sample name	Old name
NL1	LS048
NLC1	LS054
NLC2	LS048-Cu
NLC2	LS058
NLCP	LS058-Pt
LP1	Pt-01
LP2	Pt-02
NLP1	LS063

Table A.2: Sample names.

NL1 / NGO|LSMO(10nm)

This sample was cut into pieces called NL1-3(s), 4(s) and 6(m). More information about these is available in table A.3 below.

NLC1 / NGO|LSMO(13nm)|Cu(10nm)

This sample was cut into NLC1-m1 and m2. More information about these is available in table A.4 below.

Sample	Dimensions (mm)
NL1-3(s)	2.30 × 1.90
NL1-4(s)	2.30 × 2.15
NL1-6(m)	2.10 × 2.10

Table A.3: Basic information about the NL1 samples.

Sample	Dimensions (mm)
NLC1-m1	2.10 × 2.10
NLC1-m2	2.00 × 2.05

Table A.4: Basic information about the NLC1 samples.

NLC2 / NGO|LSMO(13nm)|Cu(10nm)

The NLC2 samples have the same dimensions as the NL1 samples.

NLC3 / NGO|LSMO(10nm)|Cu(10nm)

Table A.5 shows information about the NLC3 piece.

Sample	Dimensions (mm)
NLC3-m	2.10 × 2.00

Table A.5: Basic information about the NLC3 sample.

NLP1 / NGO|LSMO(?nm)|Pt(?nm)

Table A.6 shows information about the NLP1 piece.

Sample	Dimensions (mm)
NLP1-m1	2.05 × 2.00

Table A.6: Basic information about the NLP1 sample.

Appendix B

Per-sample growth parameters

All LSMO layers were, after growth, cooled in vacuum. Cu and Pt layers were grown in Ar atmosphere.

NL1 / NGO|LSMO(13nm)

Parameter	LSMO layer	Cu layer
Temperature (°C)	840	100
Pressure (mbar)	2.2	0.6
Flow (sccm)	47.7	52.1

Table B.1: Growth parameters for the NL1 sample. The Cu layer was grown about a month later, on small pieces, ~2×2mm.

NLC1 / NGO|LSMO(13nm)|Cu(10nm)

Parameter	LSMO layer	Cu layer
Temperature (°C)	840	27
Pressure (mbar)	2.2-2.3	0.6
Flow (sccm)	43.7	54.4

Table B.2: Growth parameters for the NLC1 sample.

LC1 / LAO|Cu(10nm)

Parameter	Cu layer
Temperature (°C)	100
Pressure (mbar)	0.6
Flow (sccm)	52.1

Table B.3: Growth parameters for the LC1 sample.

NLC3 / NGO|LSMO(10nm)|Cu(10nm)

The Pt layer was grown later in an external system, a Laybold-Heraeus Z-400, at room temperature and with an Ar flow of 50 sccm.

Parameter	LSMO layer	Cu layer
Temperature (°C)	840	100
Pressure (mbar)	2.2-2.3	0.58
Flow (sccm)	43.2	~50

Table B.4: Growth parameters for the NLC3 sample.

LP1 / LAO|Pt(11.5nm)

Parameter	Pt layer
Temperature (°C)	400
Pressure (mbar)	1
Flow (sccm)	52.4

Table B.5: Growth parameters for the LP1 sample.

LP2 / LAO|Pt(?nm)

Parameter	Pt layer
Temperature (°C)	250
Pressure (mbar)	1
Flow (sccm)	52.8

Table B.6: Growth parameters for the LP2 sample.

NLP1 / NGO|LSMO(?nm)|Pt(?nm)

Parameter	LSMO layer	Pt layer
Temperature (°C)	840	250
Pressure (mbar)	2.2	1
Flow (sccm)	42.4	52.8

Table B.7: Growth parameters for the NLP1 sample.

References

[1] S. Murakami, N. Nagaosa, and S. Zhang, "Dissipationless quantum spin current at room temperature," *Science*, vol. 301, no. 5638, pp. 1348–1351, 2003.

[2] C.-Q. Jin, J.-S. Zhou, J. Goodenough, Q. Liu, J. Zhao, L. Yang, Y. Yu, T. Katsura, A. Shatskiy, and E. Ito, "High-pressure synthesis of the cubic perovskite $BaRuO_3$ and evolution of ferromagnetism in $ARuO_3$ (A = Ca, Sr, Ba) ruthenates," *PNAS*, vol. 105, no. 20, pp. 7115–7119, 2008.

[3] O. Chmaissem, B. Dabrowski, S. Kolesnik, J. Mais, J. Jorgensen, and S. Short, "Structural and magnetic phase diagrams of $La_{1-x}Sr_xMnO_3$ and $Pr_{1-y}Sr_yMno_3$," *Phys. Rev. B*, vol. 67, no. 094431, 2003.

[4] A. Urushibara, Y. Moritomo, T. Arima, A. Asamitsu, G. Kido, and Y. Tokura, "Insulator-metal transitions and giant magnetoresistance in $La_{1-x}Sr_xMnO_3$," *Phys Rev. B*, vol. 51, no. 20, pp. 14103–14109, 1995.

[5] M. Bowen, M. Bibes, A. Barthélémy, J.-P. Contour, A. Anane, Y. Lemaître, and A. Fert, "Nearly total spin polarization in $La_{2/3}Sr_{1/3}MnO_3$ from tunneling experiments," *Appl. Phys. Lett.*, vol. 82, no. 233, 2003.

[6] R. Soulen, M. Osofsky, B. Nadgomy, T. Ambrose, P. Broussard, S. Cheng, J. Byers, C. Tanaka, J. Nowack, J. Moodera, G. Laprade, A. Barry, and M. Coey, "Andreev reflection: a new means to determine the spin polarization of ferromagnetic materials," *J. Appl. Phys*, vol. 85, no. 4589, 1999.

[7] H. Boschker, M. Mathews, E. Houwman, H. Nishikawa, A. Vailionis, G. Koster, G. Rijnders, and D. Blank, "Strong uniaxial in-plane magnetic anisotropy of (001)- and (011)-oriented $La_{0.7}Sr_{0.3}MnO_3$ thin films on $NdGaO_3$ substrates," *Phys. Rev. B*, vol. 79, no. 214425, 2009.

[8] Z. Celinski, K. Urquhart, and B. Heinrich, "Using ferromagnetic resonance to measure the magnetic moments of ultrathin films," *J. Mang. Magn. Mater.*, vol. 166, pp. 6–26, 1997.

[9] S. Mizukami, D. Watanabe, M. Oogane, Y. Ando, Y. Miura, M. Shirai, and T. Miyazaki, "Low damping constant for Co_2FeAl Heusler alloy films and its correlation with density of states," *J. Appl. Phys.*, vol. 105, no. 07D306, 2009.

[10] Y. Tserkovnyak and A. Brataas, "Enhanced Gilbert damping in thin ferromagnetic films," *Phys. Rev. Lett.*, vol. 88, no. 11, pp. 117601–117605, 2002.

[11] R. Urban, B. Heinrich, and G. Woltersdorf, "Semiclassical theory of spin transport in magnetic multilayers," *J. Appl. Phys*, vol. 93, no. 8280, 2003.

[12] K. Ando, S. Takahashi, J. Ieda, H. Kurebayashi, T. Trypiniotis, C. Barnes, S. Maekawa, and E. Saitoh, "Electrically tunable spin injector free from the impedance mismatch problem," *Nature Materials*, vol. 10, pp. 655–659, 2011.

[13] M. Belmeguenai, S. M. an C. Adamo, L. Méchin, C. Fur, P. Monod, P. Moch, and D. Schlom, "Temperature dependence of magnetic properties of $La_{0.7}Sr_{0.3}MnO_3/SrTiO_3$ thin films on silicon substrates.," *Phys. Rev B.*, vol. 81, no. 5, p. 054410, 2010.

[14] S. Mizukami, Y. Ando, and T. Miyazaki, "The study on ferromagnetic resonance linewidth for NM/80Fe/NM (NM = Cu, Ta, Pd and Pt) films," *Jpn. J. Appl. Phys*, vol. 40, pp. 580–585, 2001.

[15] M. D'Yakonov and V. Perel, "Possibilty of orienting electron spins with current," *Sov. Phys. JETP Lett.*, vol. 13, p. 467, 1971.

[16] J. Hirsch, "Spin Hall effect," *Phys. Rev. Lett.*, vol. 83, no. 9, pp. 1834–1837, 1999.

[17] E. Saitoh, M. Ueda, H. Miyajima, and G. Tatara, "Conversion of spin current into charge current at room temperature: Inverse spin-Hall effect," *Appl. Phys. Lett.*, vol. 88, no. 182509, 2006.

[18] S. Maekawa, "Magnetism: A flood of spin current," *Nature Materials*, vol. 8, pp. 777–778, 2009.

[19] "Freie Universität Berlin, Fachbereich Physik website." `http://www.physik.fu-berlin.de/einrichtungen/ag/ag-kuch/research/techniques/fmr.html`.

[20] A. Francis, Y. Cao, and P. Salvador, "Epitaxial growth of Cu(100) and Pt(100) thin films on perovskite substrates," *Thin Solid Films*, vol. 496, no. 2, pp. 317–325, 2005.